Nuclear Materials and Energy 45 (2025) 102011

Contents lists available at ScienceDirect

Nuclear Materials and Energy

journal homepage: www.elsevier.com/locate/nme

Investigating the microstructure of additively manufactured tungsten parts produced by electron beam powder bed fusion process

Miguel Zavala-Arredondo [a,*], Arun Ramanathan Balachandramurthi [b,c], Lidija Stjepanic Peric [b], Nick Weston [d], Katy Rankin [e], Sebastian Rosini [a], Khurram Amjad [a], Jeong-Ha You [f]

[a] UKAEA, 2A Lanchester Way, Advanced Manufacturing Park, Rotherham S60 5FX, UK
[b] Freemelt AB, Bergfotsgatan 5a, Moelndal 43135 SE, Sweden
[c] Wallenberg Initiative Materials Science for Sustainability, Department of Science and Technology, Linköping University, Norrköping 601 74, Sweden
[d] Royce at the University of Sheffield, School of Chemical, Materials and Biological Engineering, Royce Discovery Centre, Harry Brearley Building, 5 Portobello Street, S1 4ND, UK
[e] University of Southampton, Faculty of Engineering and Physical Sciences, Southampton SO17 1BJ, UK
[f] IPP (Max Planck Institute for Plasma Physics), Garching, Germany

ARTICLE INFO

Keywords:
Additive manufacturing
Electron beam powder-bed-fusion
Spot melting
Pure tungsten
Hot isostatic pressing
Microstructure
Crystallographic orientation

ABSTRACT

Pure tungsten is one of the promising candidate materials for plasma facing components (PFC) of future fusion reactors due to several favourable properties including its high melting point, high thermal conductivity, high strength, high sputtering resistivity and low coefficient of thermal expansion. Increasing geometric complexity and productivity of tungsten PFC is of interest to improve thermal performance and availability for new tokamaks with a view to future steady state plasma operation. Additive manufacturing (AM) by the electron beam powder-bed-fusion process (EB-PBF) is identified as a potential technology to address these requirements. In this paper we reviewed the literature in EB-PBF of unalloyed tungsten to understand the role that the manufacturing parameters have in the microstructure and mechanical performance of as-printed specimens. We present targeted key research in tungsten EB-PBF process development using a modulated point melting method, post-AM hot isostatic pressing (HIP) treatment, destructive and non-destructive evaluation, microstructure control, and in-process monitoring. It was found that the modulated point melting method reduces cleavage cracking and crack nucleation points while elevated temperature HIP treatment improves the repeatability of the tensile behaviour, while mechanically healing process induced defects like solid-state cracks and nanopores.

1. Introduction

Tungsten (W) is a refractory metal with extraordinary resistance to heat and wear. It has the highest melting temperature of all known metals in pure form (3420 °C), high density, high thermal conductivity, high strength and hardness, and excellent mechanical properties at elevated temperatures. Further, W offers high resistance against sputtering, low tritium retention in fusion environments, and better neutron irradiation performance compared to other high melting refractory metals [1]. Due to its material properties, W has numerous applications

Abbreviations: AM, Additive Manufacturing; BCC, Body Centred Cubic; BSE, Backscatter Electron; CPS, Capillary Porous Structure; DBTT, Ductile-to-Brittle Transition Temperature; DIC, Digital Image Correlation; EB-PBF, Electron Beam Powder Bed Fusion; EBSD, Electron Backscatter Diffraction; EDM, Electrical Discharge Machining; ELO, Electron Optical Imaging; FEMU, Finite Element Model Updating; FSD, Forward Scatter Detector; HAGB, High Angle Grain Boundary; HF, Hot Forging; HIP, Hot Isostatic Pressing; HP/HS-RS High-Power, High-Speed Raster Scanning; HR, Hot Rolling; IEK, Institute of Energy and Climate Research; IPF, Inverse Pole Figure; KIT, Karlsruhe Institute of Technology; L-DED, Laser Directed Energy Deposition; L-PBF, Laser Powder Bed Fusion; NCSU, North Carolina State University; NDE, Non-Destructive Evaluation; NH, No HIP-treatment; NIN, Northwest Institute for Nonferrous Metal Research; ORNL, Oak Ridge National Laboratory; PBF, Powder Bed Fusion; PEP, Powder Extrusion Printing; PFM, Plasma Facing Material; PIP, Profilometry-based Indentation Plastometry; PKU, Peking University; PMI, Plasma-Material Interaction; RS, Raster Scanning; RT, Room Temperature; SEM, Scanning Electron Microscopy; SDS, Single Directional Shifted; SDS/PH, Single Directional Shifted Point Heating; SS, Stainless Steel; TUOS, The University of Sheffield; UTS, Ultimate Tensile Strength; W, Tungsten; XCT, X-ray Computed Tomography; X-EDS, Energy-Dispersive X-ray Spectroscopy.

* Corresponding author.
E-mail address: miguel.zavala-arredondo@ukaea.uk (M. Zavala-Arredondo).

https://doi.org/10.1016/j.nme.2025.102011
Received 31 July 2025; Received in revised form 30 September 2025; Accepted 14 October 2025
Available online 17 October 2025

ranging from medical to transport, energy, defence, and other industry sectors [2]. However, there are still some drawbacks limiting practical use of W-based materials such as low oxidation resistance, low ductility at room temperature (RT) and high ductile-to-brittle transition temperature (DBTT) [1].

In the fusion reactor, in-vessel plasma facing materials (PFMs) are used in the divertor and breeder blanket [3], with W considered as one of the most promising PFMs for high heat flux applications [4]. Full W divertors consisting of Monoblock units are being designed and installed in existing and new tokamaks with a view to future steady state plasma operation [5,6]. Further, conceptual designs for future liquid–metal divertors are being considered with additively manufactured W capillary porous systems (CPS) which may offer improved performance compared to the conventional W Monoblock concept [7,8].

Electron beam powder-bed-fusion (EB-PBF) is an additive manufacturing (AM) technology that is increasingly attracting academic and industry attention, in part due to its high-temperature capability for processing difficult materials such as W and W-based alloys [9]. It is currently considered the most viable AM technology for manufacturing W components with acceptable strength. Other AM technologies investigated for W components include laser powder-bed-fusion (L-PBF), laser directed-energy-deposition (L-DED), and powder extrusion printing (PEP) [10,11]. However, these typically offer reduced mechanical performance for W printed parts compared to EB-PBF technology. Due to EB-PBF process characteristics, this technology has increasingly been investigated for producing functional W parts with complex geometries for high heat flux applications since thermo-mechanical properties of W EB-PBF material have shown comparable performance to those of ITER grade tungsten [12,13].

The present work investigates the state-of-the-art in W EB-PBF process development to understand the effect of manufacturing parameters in the microstructure and mechanical performance of this material. Process conditions with novel melting strategies are explored to control microstructure and cracking. Post-AM hot isostatic pressing (HIP) treatment is investigated to elucidate its role in reducing process induced defects in the printed parts, and its effect in mechanical performance and microstructure. It is concluded that point melting method can reduce crack nucleation points whilst HIP treatment can mechanically heal cracks. This was achieved by spot melting reducing crack nucleation points in boundaries of grains with different orientation angle and around regions of {111} crystallographic orientation, while increasing surface area of {001} orientation where cracks are passivated and mechanically healed by HIP treatment. For the body centred cubic (BCC) W-lattice, which is typically closely packed along the ⟨111⟩ directions, larger surface area oriented in {001} is expected to promote gradual transition from elastic to plastic behaviour and higher work hardening [14]. Increased work hardening capacity and reduced hardness was achieved with increasing HIP temperature, which is desired to improve material ductility, a key concern for long-term structural integrity of future tungsten based divertor concepts [15].

Nanohole formation on tungsten surfaces exposed to plasmas is a critical, undesirable plasma-material interaction (PMI) mechanism that can promote nanostructured fuzz layers [16,17] which ultimately generate tungsten dust that contaminates the plasma. The EB-PBF melting strategies and process parameters investigated in the present work were observed to promote (001) crystallographic orientation across the process layers and along the build direction in the printed parts. This offers great potential to improve the PMI performance in EB-PBF W plasma facing components (PFCs) as tungsten surfaces with predominantly (001) orientation can reduce nanohole density and size under helium plasma exposure [18]. On the other hand, spot melting was observed to develop controlled localised regions with (111) orientation. This offers potential to tailor local crystallographic orientation by developing advanced spot melting strategies to improve local resistance to irradiation-induced damage like embrittlement and hardening after helium implantation [15,19,20].

It is known that thermal conductivity of EB-PBF W material can match that of rolled W [13] and [13] is further increased by elevated temperature HIP treatment [21] while leveraging higher geometric complexity [13,22]. It is suggested to consider HIP-treated EB-PBF W material for development of new PFC designs in applications where strength is a viable compromise that can be reduced to improve geometric complexity and crystallographic orientation control, e.g., to improve thermal and PMI performance of conventional W Monoblock designs [23].

The structure of the paper is composed by four main sections including background, experimental methodology, results and discussion, and conclusions. The ‘background’ section presents the state-of-the-art in EB-PBF process development and compares the mechanical performance and microstructure of EB-PBF W specimens reported in the literature. The ‘results and discussion’ section is presented in different sub-sections investigating mechanical properties and its relationship with the microstructure of test specimens; characteristics of internal defects by means of destructive and non-destructive evaluation methods; and the effect of varying EB-PBF parameters and melting strategies in the microstructure and cracking control.

2. Background

2.1. EB-PBF process development

In the last decade, EB-PBF machine development driven by original equipment manufacturers have seen remarkable growth as many new companies entered the market offering unique system advantages [24]. EB-PBF process development led by key research organisations around the world has improved the quality and performance of AM W material for potential fusion applications [12,22,25,26,27,28,29,30,31].However, most of the published research has been conducted in different variations of one single commercial system. New machine developments from different commercial EB-PBF platforms have the potential to offer different capabilities that can assist W processing. As shown in [24], each machine available in the market has different technical characteristic and offers special advantages that have not been fully investigated in the literature. The present work investigates some of these special advantages using the Freemelt platform.

Table 1 shows examples of EB-PBF process parameters developed by different research organisations to produce tungsten parts with minimal porosity and reduced cracking. It is known that different parameters and manufacturing conditions produce parts with different microstructure and mechanical properties.

2.2. Mechanical performance and microstructure

NIN [25] and PKU [29] conducted compressive testing in EB-PBF W parts. Both observed typical columnar grain structures that form along the build direction. NIN reported columnar grain widths ranging from 50 to 100 μm, whilst PKU reported columnar grain width up to 320 μm. Typically, finer microstructures are desired to improve strength [32]. However, the coarser microstructure by PKU showed higher compressive strength.

Coarser microstructures indicate reduced residual stress build-up during the printing process [33]. It is suggested that grain size in EB-PBF W specimens has positive correlation with compressive strength-strain performance due to reduced residual stress formation. For instance, the main processing difference between NIN and PKU is the preheating temperature and the use of different baseplate materials, namely: W and SS 316, respectively (see Table 1). Higher preheating temperature is expected to reduce thermal gradients, in turn reducing residual stress build-up in the EB-PBF melting process [34]. On the other hand, substrates with lower yield can reduce residual stresses as thermal shrinkage is compensated by the substrate plastic deformation [33]. Preheating temperature of 1150 °C and the use of SS 316 substrate are

Table 1
Optimised EB-PBF melting parameters reported in the literature for additive manufacturing of pure W components.

	NIN (2019)	TUOS (2020)	IEK (2021)	ORNL (2021)	PKU (2022)	ORNL (2023)	NCSU (2023)	KIT (2024)
Preheating temperature (°C)	800–950	1000	1000	1500	1150	1800	1800	1000
Baseplate material	W	SS	Steel	Ti-6Al-4 V	SS 316	W	W	–
Layer thickness (μm)	50	30	50	70	50	70 [a]	70	50
Hatch offset (μm)	50	250	100	33	100	30	30	100[c]
Beam current (mA)	16	8	–	21	15	12	10	14
Voltage (kV)	60	50	–	60 [a]	60	60	–	–
Beam power (W)	960	400	900	1260[b]	900	720	–	–
Focus offset (mA)	–	10	–	40	–	–	10	10
Spot size (μm)	200	–	300	–	250	–	–	–
Beam speed (mm/s)	100	130	180	456	180	359	300	225
Line energy density (J/mm)	9.6	3.1	5.0	2.8	5.0	2.0	–	–
Areal energy density (J/mm^2)	192	12.3	50.0	83.7	50.0	66.9	–	–
Volumetric energy density (J/mm^3)	3840	410	1000	1196	1000	955	–	–

[a] Values taken from work by the same authors in [28] and [27].
[b] Derived from the product of beam current and voltage.
[c] Value assumed from previous work by the authors in [12].

expected to reduce thermal gradients, cooling rates and residual stresses in the specimens produced by PKU, in comparison with those produced by NIN which used only 800–900 °C preheating temperature and a tungsten substrate. Note: tungsten material theoretically exhibits thermal conductivity and yield strength of 170 W/m•K and 750 MPa, respectively, compared to 16.3 W/m•K and 205 MPa for SS 316.

ORNL [22] and KIT [13] investigated the tensile performance of EB-PBF W specimens under inert and vacuum conditions, respectively. They conducted elevated-temperature tensile testing of specimens printed in longitudinal and transverse directions relative to the build direction. As expected, both observed high anisotropy in the tensile performance, due to a characteristic columnar grain structure that is formed along the build direction. KIT explained that sample preparation through wire electrical discharge machining (wire-EDM) can cause external damage to the test specimen, introducing apparent porosity and cracking across the whole sectioned surface. They suggested that the samples must be carefully prepared prior tensile testing by grinding, mechanical polishing, and subsequent electrochemical polishing. Such careful sample preparation process is expected to improve the mechanical performance by reducing defects at the sectioned surface, which may explain the outstanding tensile strain of about 80 % achieved by KIT.

It is known that wire-EDM process causes cracking in the sectioned faces of single crystal tungsten, particularly along {001} planes [14]. In the present research, the damage caused by wire-EDM cutting process during preparation of EB-PBF W samples is investigated. It is demonstrated that wire-EDM significantly degrades the quality of EB-PBF W parts, which show {001} orientation predominance. This damage is expected to cause premature failure and reduce mechanical performance.

ORNL reported higher tensile strength in transverse specimens (i.e., printed horizontally) in comparison to the KIT experiments. From Table 1, it is noted that ORNL used smaller hatch offset (distance between raster-scan tracks), which is known to reduce local thermal gradients, cooling rates, and residual stresses [27]. Additionally, ORNL almost doubled the preheating temperature which is expected to further reduce residual stress formation. This can explain the coarser microstructure observed in ORNL specimens (note: KIT reported columnar grain width ranging from 50 to 100 μm, while ORNL show micrographs where columnar grain widths can be measured in the range of about 100–300 μm [22]). It is thought that lower residual stress formation in the ORNL samples resulted in higher tensile strength in comparison with the KIT results.

It is known that cooling rates and grain size have negative correlation [35]. Finer microstructures are associated with higher cooling rates and higher residual stress build-up in EB-PBF W material. From comparing results reported in the literature, it is concluded that EB-PBF parameters that develop coarser microstructures have the potential to improve the compressive and tensile strength of as-manufactured EB-PBF W specimens [13,22,25,29]. It is thought that such improvement is mainly due to lower residual stress formation during the printing process.

It must be noted that post-AM thermal treatments or HIP treatments and their effect on the mechanical performance of EB-PBF W parts have not been investigated before. Typically, HIP treatment is used in other AM materials to improve the tensile elongation while subsequent heat treatment is needed to increase the tensile strength [36]. The present work investigates the effect of HIP treatment alone in the tensile performance of EB-PBF W specimens. A post-AM grain coarsening effect is observed with increasing HIP temperature, which describes a change in the tensile deformation behaviour.

Finally, KIT demonstrated that tensile specimens printed horizontally (with the tensile load pulling in transverse direction relative to the build direction) have higher DBTT than specimens printed vertically (with tensile load longitudinal to the build direction) [13,40]. This is in part due to high tensile residual stresses that promote cracking in conventional raster scanning methods [37]. As cracks grow transversally across the raster scanning vectors [38,39], the tensile performance of horizontal specimens (which have the tensile load direction parallel to the direction of scanning vectors) is reduced in comparison with vertical specimens.

It is concluded that new EB-PBF melting strategies are needed to reduce thermal gradients and cooling rates typically developed in conventional raster-scanning melting methods. This can help reduce anisotropy in the mechanical performance by reducing crack formation and crack propagation in both transverse and longitudinal planes relative to the build direction. The present work investigates EB-PBF process development using spot melting Pixelmelt® technology to address typical processing challenges currently limiting AM of unalloyed tungsten. Different process parameters and melting strategies are researched to understand their effect on the microstructure and mechanical performance of AM parts. Finally, the effect of HIP treatment is investigated as potential post-AM process to mitigate EB-PBF process induced defects, close solid-state cracks, and improve repeatability.

3. Experimental methodology

3.1. Tungsten powder characteristics

Plasma spherodised pure tungsten powder from 6 K Additive with

Table 2
Chemical composition of W powder.

Element	Cr	Fe	Mo	Ni	O	Ta	W
Wt. %	<0.01	0.01	<0.01	0.01	0.008	<0.01	Bal. (~99.9)

particle size distribution of 45–106 μm was used in the present research. The chemical composition is presented in Table 2.

3.2. EB-PBF process and fabrication of test specimens

A Freemelt One system was used to investigate three different EB-PBF melting strategies using Pixelmelt® technology. These are denominated raster scanning (RS), high-power/high-speed raster scanning (HP/HS-RS), and single directional shifted-point heating strategy (SDS-PH). The SDS-PH beam path is equivalent to that shown for the "Point Heat Source Fill" strategy described in [40]. SDS-PH is used here applying a beam adjustment sequence at each point as described in [41]. The need for such beam modulation is to affect the heating/cooling rates at each point to lower the local thermal gradient. The idea of the SDS-PH strategy is to investigate the potential of a modulated point heating method to control grain growth and cracking. Fig. 1 shows example of the beam modulation method used in SDS-PH strategy.

Process parameters were developed for the different melting strategies to minimise porosity at the core of the part. Development of contour parameters (i.e., applied at border regions in the part) is out of scope in the present research.

Multiple builds were completed to produce parts for the different melting strategies. Four parts were printed per build and one single strategy was used on each build. Tungsten baseplates were used for all strategies. To mitigate radiative cooling effect, the melting order of the parts in consecutive layers follows a circular rolling order 1:2:3:4:: 2:3:4:1:: 3:4:1:2:: 4:1:2:3:: 1:2:3:4 and so on. Table 3 shows the process parameters used for each melting strategy.

Four EB-PBF bars were produced with dimensions 15 × 15 × 85 mm using RS parameters. After removing the bars from the baseplate, HIP treatment was applied to three bars at 150 MPa and 4 h dwell time, and one bar was kept in the as-printed condition with no HIP-treatment applied. Each HIP-treated bar was processed separately using different HIP temperatures: 1400 °C, 1600 °C, and 1800 °C, respectively. Miniaturised dog-bone tensile specimens with dimensions of about 25 × 5 × 1 mm were extracted at bottom and top regions from the EB-PBF RS bars using wire-EDM process. Tensile specimens extracted from bottom and top regions were denominated batch 1 (b1) and batch 2 (b2), respectively. Wire-EDM was also used to extract 1 × 1 × 76 mm matchstick samples and 10 × 10 × 10 mm cubes for XCT scanning and profilometry-based indentation plastometry (PIP), respectively. One additional bar was printed in a separate build using the same RS parameters, and cross-sectioned using disk cutting process to compare against specimens sectioned by wire-EDM process.

To investigate the microstructure of different melting strategies, four EB-PBF bars were produced using HP/HS-RS strategy in one build, and four using SDS-PH strategy in a separate build. These were HIP-treated at three different temperatures, and one sample was kept in the as-printed condition for each build. Same HIP parameters were used as with the RS bars. The bars were sectioned using wire-EDM and disk cutting processes.

Table 3
EB-PBF process parameters investigated for the different melting strategies.

	RS	HP/HS-RS	SDS-PH
Beam power	900 W	2000 W	1200 W
Beam speed	150 mm/s	1200 mm/s	–
Dwell time	–	–	3500 μs
Spot size	270 μm	270 μm	270 μm
Scan strategy	Hatching with unidirectional lines	Hatching with unidirectional lines	Spot melting
Line offset	100 μ m	100 μ m	–
Point spacing	–	–	225 μ m
Layer thickness	75 μ m	75 μ m	75 μ m
Scan rotation	90°	90°	90°
Process temperature	1000 °C	1200 °C	1200 °C

3.3. Material characterisation

EB-PBF W specimens were sectioned using wire-EDM and abrasive sectioning methods for comparison. Optical, Scanning Electron (SEM) and electron backscatter diffraction (EBSD) microscopy were used to investigate microstructure. Abrasive sectioning was achieved using equipment (Struers Secotom-50) and a Struers M0D15 diamond cut-off blade. Once sectioned, the samples were hot mounted in Struers Duro-Fast thermosetting epoxy. Surface preparation was achieved by following the steps in Table 4, then thoroughly cleaning with water and isopropanol, and completely drying. For samples undergoing EBSD, they were broken out of the hot mount and attached to a 5 mm × 12.5 mm diameter mounting stub with silver electrodag.

For creation of light micrograph mosaics, the entire surface of each prepared and mounted sample was imaged as a series of individual micrographs using an Olympus Bx51 light microscope equipped with a Clemex Vision PE image analysis system and software. The software ImageJ was then used to correct these micrographs for uneven background illumination, stitch them together into a mosaic, and enhance the brightness and contrast. Relative densities were calculated measuring porosity by pixel count from micrograph mosaics of the entire surface of the samples using ImageJ software.

For SEM/EBSD/X-EDS investigation, the prepared and mounted samples were then investigated using a JEOL JSM-7900F Schottky Field Emission Scanning Electron Microscope. This system allows Secondary Electron (SE) Imaging and subsequent concurrent collection of EBSD crystal structure and EDS elemental identification data. Maps were performed at several magnifications and a variety of locations around the centre and edges of the samples to attempt to capture features of interest. The software was asked to detect the body-centred-cubic α phase of tungsten and some of the more common tungsten oxides (WO3, WO2, W18O49, W10O29) using inbuilt pre-set data on the structure of those phases. The composition of the samples is nominally pure tungsten, since it was processed under vacuum, but the possibility for trace contamination of oxygen and/or carbon exists, so the software was set to detect these elements (W, O, C). No contamination was observed.

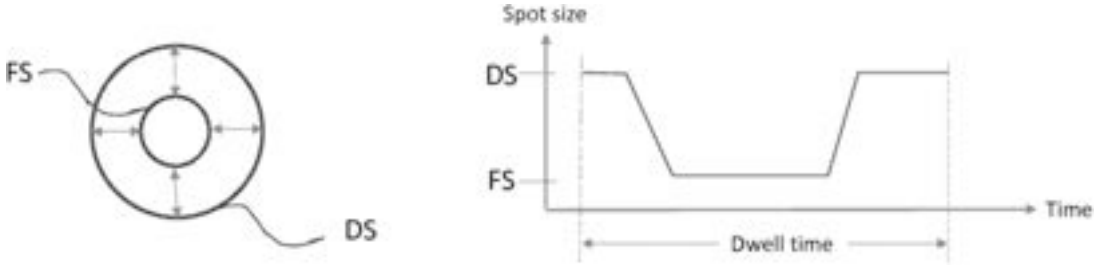

Fig. 1. Beam adjustment sequence used in the SDS-PH strategy. The electron beam spot size changes from a defocused spot (DS) to a focused spot (FS) and vice versa, as a step function over time. This is applied on each spot in the SDS-PH beam path [41].

Table 4
Details of the metallographic preparation route.

Step	Surface	Abrasive	Platen Speed	Head Speed (rpm)	Comp/contra	Lubricant	Force (N)	Time (min)	Quantity
1	SiC Foil	P800	250	50	Comp	Water	25	1:00/sheet	x6
2	SiC Foil	P1200	250	50	Comp	Water	25	1:00/sheet	x5
3	SiC Foil	P2500	250	50	Comp	Water	25	1:00/sheet	x5
4	Struers MD-Dac	3 μm Metprep Diamet Susp.	180	60	Contra	N/A	25	10:00	x1
5	Struers MD-Dac	1 μm Metprep Diamet Susp.	150	60	Contra	N/A	25	7:30	x1
6	Struers MD-Chem	0.04 μm OP-US colloidal silica	150	60	Contra	N/A	35	5:00	x1

3.4. EB-PBF process monitoring and XCT scanning

Backscatter electron (BSE) imaging was used as process monitoring technique in EB-PBF builds. BSE images were captured layer by layer during the printing process. Porosity in EB-PBF layers was measured from BSE images by pixel count using ImageJ software. X-ray computed tomography (XCT) was used to scan W matchstick specimens at 1.89 μm voxel resolution, with ultimate spatial resolution of about 3 μm. Around 17 scans were used to cover the full 76 mm length of these specimens. Scans were carried out using a diondo d5 system (diondo GmHb, Germany). The X-ray source energy and current were set to 290 kVp and 40 μA, respectively, and a 0.5 mm thick Sn pre-filtration of the x-ray beam was used to mitigate beam hardening artefacts. The source to object and source to detector distances were set to 9.5 mm and 700 mm, respectively. Tomographic reconstruction was carried out using filtered back-projection implemented via the Siemens CERA toolbox (Siemens Healthineers AG, Germany).

3.5. Mechanical testing

Only samples produced by conventional raster scanning (RS) method were used for mechanical testing. The samples were tested in the as-cut condition, after wire-EDM cutting. The metallographic preparation route described in Table 4 could not be applied to the tensile specimens. Therefore, any damage caused by the wire-EDM process could not be removed.

Tensile testing was conducted at room temperature and at 550 °C. Digital image correlation (DIC) was used to determine sample gauge extension to generate stress–strain curve. The experimental setup consisted of a 10kN Instron universal test machine equipped with an environmental chamber (Severn Thermal Solutions Ltd, UK) capable of reaching a maximum operating temperature of 600 °C. An Inconel sheathed heating element heated the chamber, which was separated from the inner chamber by a stainless-steel baffle. A PID temperature controller (Eurotherm, UK) and a K-type thermocouple mounted in front of the baffle controlled the chamber temperature. A fan circulated hot air in the chamber for uniform heating. An additional K-type thermocouple was fed through the instrument port at the top of the chamber and affixed to the grips of the tensile test sample as means of monitoring the bulk material temperature. To facilitate calibration of the stereo camera setup through the door window, the chamber featured a fully detachable lift-off door. The door was supported by a constant spring attached to the machine columns. The chamber was mounted on the guide rails of a trolley, allowing it to be moved rearwards away from the sample space. This enabled calibration to be performed through the door window with the door in place.

A stereo-camera setup from LaVision GmbH was used for measuring sample displacements over the sample gauge section during tensile loading, which consisted of a pair of 12-bit digital cameras with a CMOS sensor of 2056 × 2464 pixels^2, fitted with 200 mm Nikon macro lenses. The cameras were mounted on a tripod at a stand-off distance of 45 mm in front of the chamber window providing an effective spatial resolution of 145 pixels/mm. An LED light array (GSVitec GmbH) was used for illumination, configured to trigger in-sync with the camera image capture. To minimize specular reflections from the chamber window, LED array was covered with a linear polarising film and circular polarisers were mounted onto the camera lenses. Photograph of the experimental setup is provided in Fig. 2 and parameters for the stereo-DIC setup and image correlation are provided in Table 5.

Elevated temperature PIP (ET-PIP) was used to evaluate performance of different EB-PBF W specimens relative to each other. The PIP method is based on iterative Finite Element Model Updating (FEMU) simulation of the indentation process, converging on a best-fit set of parameter values in a constitutive law describing the stress–strain relationship [42]. Indents were made at 550 °C using the PLX-HotStage setup. Heating to 550 °C took around 5 min, and a soak time of 3 min at 550 °C was used to allow for temperature stabilisation. Prior to indentation, the indented surfaces were prepared to a 1 μm polished surface finish. It should be noted that this degree of surface preparation is higher than is typically required for an accurate PIP test which only requires a P1200 grind. However, polishing to a mirror finish has the advantage of allowing examination of the microstructure surrounding an indent. This microstructure can provide insight into the deformation processes occurring during indentation, as well as giving an indication of grain size and any sample anisotropy. Indenters of 1 mm and 0.5 mm radius were used for samples exhibiting grains of about 600 μm (e.g., HIP-1800 samples) and 200 μm (e.g., NH and HIP-1600 samples) respectively. Three samples were successfully tested to derive full nominal stress–-strain curves up to the point of necking.

4. Results and discussion

4.1. In-process monitoring

Back scatter electron imaging (BSE), also known as electron optical imaging (ELO), was used to monitor the build process [43]. BSE was effectively used to predict part quality by conducting non-destructive evaluation (NDE) of % porosity layer by layer in the core region of the

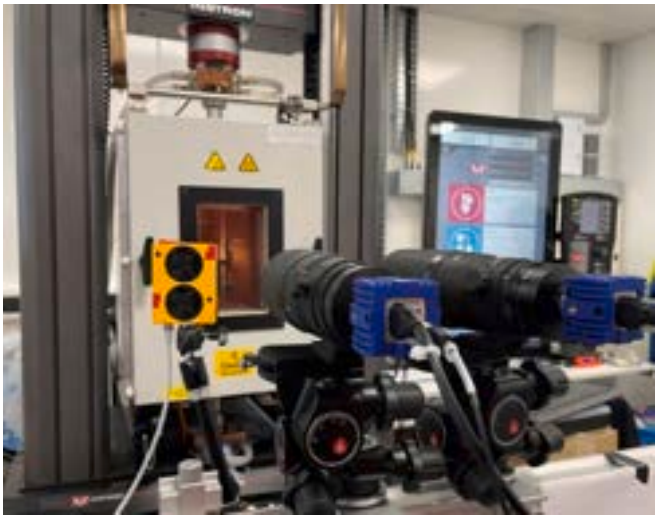

Fig. 2. Experimental setup for measuring sample gauge displacements during tensile testing using digital image correlation technique.

Table 5
Details of stereo-DIC setup and correlation parameters.

Stereo-DIC setup details	
Cameras	12 bit, 2056 × 2464 pixels^2
Lens focal length	200 mm
Stereo angle	13°
Field of view	14.1 × 17.51 mm^2
Scale	145.33 px/mm
Image correlation details	
Software	DaVis 10.2.1 (LaVision GmbH)
Subset size	45 px
Subset spacing	10 px
Shape function	Affine
Image interpolant	Bicubic polynomial
Correlation criterion	Zero-normalised sum of square differences

part. A porous region was identified with layers transitioning from support structures to fully dense bulk material. Fig. 3 shows example of % porosity area with BSE images for illustration. The porosity of BSE images was compared with relative density measured by optical analysis from cross-section micrographs. A difference in the range of about 0.1 % to 0.2 % was obtained which suggests that 0 % porosity measured in BSE images can be used to estimate relative density in the range of about 99.8 % to 99.9 % in the as printed part. Cracking could not be captured by BSE imaging due in part to low BSE resolution relative to crack dimensions and because cracking predominantly occurs during the cooling-down process when the temperature decreases below the DBTT. Since the EB-PBF process, ambient temperature is set to ≥1000 °C, decreasing temperature below the DBTT only happens after the printing process is complete, and layer-by-layer BSE imaging is no longer possible. However, BSE is demonstrated as valuable NDE tool that can be used to quantify process-induced defect population and layer-by-layer repeatability throughout the printing process, particularly relevant for qualification of EB-PBF W components.

4.2. *Effect of wire-EDM process*

Wire-EDM damage was investigated by comparing two EB-PBF W specimens manufactured with the same printing parameters but cut using different sectioning methods. Fig. 4 shows cross-sections of a) a specimen sectioned by wire-EDM process and b) a specimen abrasively sectioned using diamond cut-off wheel disk cutting method. The specimens underwent the same metallographic preparation route (see Table 4). This showed that a layer of material with significant damage was created by the wire-EDM cutting process. It is thought that the apparent porosity is caused by pullout of cracked/fractured pieces from the structure. It is known that wire-EDM cutting produces a heat affected zone and recast layer where the material is melted by the cutting wire [44], and it is thought that the rapid cooling rate causes the tungsten to crack, inducing profuse cracking along the grain boundaries. With other metals (e.g., Ni, Ti, etc.) this recast layer is removed during standard sample preparation. However, for tungsten it is possible that either the wire-EDM damaged layer is thicker (extending as far as 100 μm or more [14]) or that less material is removed during sample preparation so that it remains visible. Removing the damage with electrochemical means is difficult due to contamination with the brass cutting wire. Alternatively, waterjet sectioning is proposed in combination with electrochemical polishing to avoid formation of critical defects in the cut section, as demonstrated in [14]. To remove the damaged layer and observe the true condition of the material, the samples were put through a second complete cycle of sample preparation, repeating steps 1–6 shown in Table 4. Fig. 4 shows example of (c) a damaged layer after 1 preparation cycle, and (d) the same sample after conducting a second preparation cycle. For samples sectioned by wire-EDM and diamond cut-off wheel, contour or subsurface porosity and lack of fusion are observed in Fig. 4a and b. Core and contour EB-PBF process parameters typically use different beam power and beam speed ratings to minimise porosity and

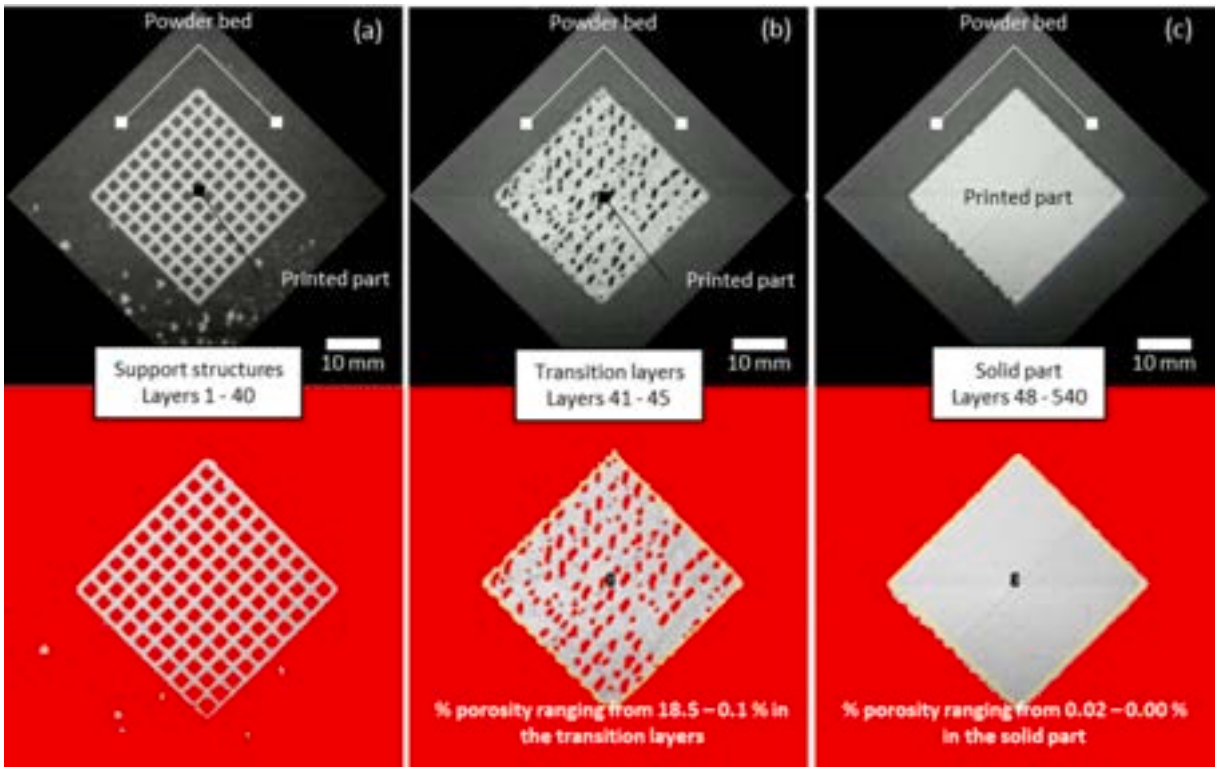

Fig. 3. Backscatter electron (BSE) images taken layer by layer during the EB-PBF process showing examples of (a) support structures, (b) transition layers, and (c) layers where the part exhibits full density. % porosity was measured by pixel count using ImageJ software.

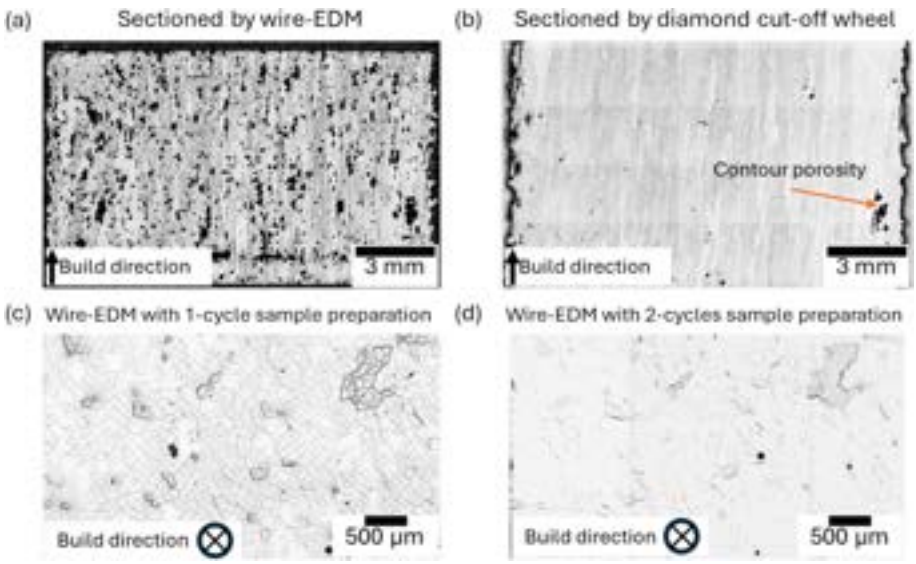

Fig. 4. Optical micrograph mosaics of samples manufactured with RS process parameters (see Table 3). The images show the effect of (a) wire-EDM process on the surface of the sample, in comparison with (b) abrasive sectioning by diamond cut-off wheel. In (a) and (b) the samples underwent the same metallographic preparation. One sample sectioned by Wire-EDM process is shown which underwent two subsequent preparation cycles. Optical micrographs were taken after (c) the first and (d) second preparation cycles, respectively.

lack of fusion at the different regions in the part [45]. Contour process parameters are out of the scope in the present research. Therefore, contour or subsurface defects are expected. The area of interest in the present investigation is the core of the part, where relative densities of about 99.93 % and 99.82 % were achieved in the transverse (XY-plane) and longitudinal (XZ-plane) sections relative to the build direction respectively.

Fig. 5 shows XCT images of a 1 mm × 1 mm × 76 mm matchstick specimen from which all 6 faces – top, bottom and side faces – were cut by wire-EDM process. Matchstick specimens were XCT-scanned from top to bottom. Top and bottom faces illustrate severe damage with evenly distributed cracking, whilst side faces show regions of pulled-out material denominated "apparent porosity", and external cracks that penetrate the core. These were induced and aggravated by wire-EDM process as the intensive electrical spark between the wire electrode and the sample causes damage to the sectioned surface and subsurface [46].

It is shown that the wire-EDM sectioning process can significantly damage external faces (e.g., bottom, sides, and top in Fig. 5), increasing the risk for potential formation of crack nucleation points at the surface. The XCT data was interrogated to estimate the depth of the wire-EDM damage. It was found that evenly distributed cracking characteristic of the wire-EDM process, can penetrate as deep as around 100 µm or more into the part, from the wire-EDM cut surface.

As external cracks penetrate the sample, the increased defect density decreases the material fracture toughness [47]. It is concluded that wire-EDM can significantly weaken EB-PBF W specimens during the sample preparation process, which significantly complicates mechanical evaluation of this material.

4.3. Effect of HIP temperature on crack size and void percentage – XCT evaluation

XCT scanning was used to evaluate EB-PBF process induced defects and the effect of HIP treatment with increasing HIP temperature. Fig. 6 shows typical transverse cracks in the XY plane (i.e., transverse to the build direction) for a) the as-printed No-HIP, and b) the HIP-1800 condition. Representative cracks observed at core regions (denominated "closed "cracks) identified in both samples are depicted in Fig. 6. Open cracks that reach the side faces are not considered since these are predominantly caused or aggravated by the wire-EDM sectioning process. It was found that crack clusters (multi-branch cracks) with long individual cracks measuring about 230–385 µm in XY length, are developed in the as-printed condition, whilst shorter individual cracks of about 121 µm-long are observed in the HIP-1800 condition. XCT scan

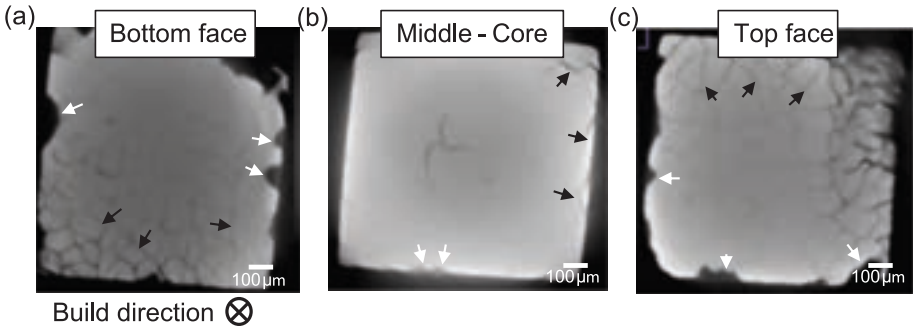

Fig. 5. XCT images taken at (a) bottom face, (b) centre, and (c) top face of a matchstick sample, extracted from a bar printed using RS parameters. Wire-EDM-induced cracking and apparent porosity are shown at (a) bottom, (a-c) side, and (c) top faces of the sample. Black and white arrows show wire-EDM induced cracks and pores, respectively. (b) Example of closed and open cracks are shown at the core of the matchstick sample. Closed crack cluster in b shows example of solid-state cracking that form during solidification at the core of the part. Open cracks shown in the side faces and profuse cracking shown at bottom and top faces are external cracks that were induced or aggravated by the wire-EDM process. These cracks penetrate the core about 100 µm deep or more. BD indicates build direction.

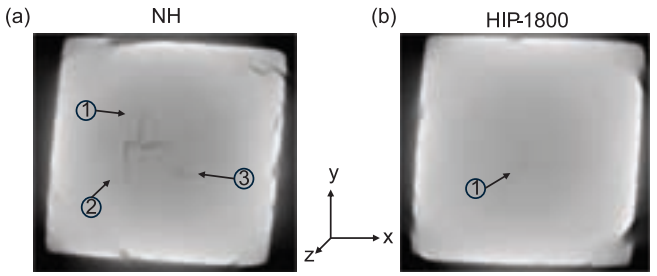

Crack #	Crack length
1	230.864 μm
2	313.840 μm
3	385.024 μm

Crack #	Crack length
1	120.586 μm

Fig. 6. XCT image of two RS samples with (a) No-HIP and (b) HIP-1800 treatment conditions. Typical cracks observed at the centre of matchstick samples are shown for the different conditions. The tables show the number of cracks and crack length for each condition. Crack lengths in XY plane are measured by pixel count using ImageJ software. Build direction is in z.

data was interrogated to calculate the crack length in the build direction, or XZ-crack length. This was done by counting the number of frames from the first frame where the crack appeared, to the last frame were the crack closed. The multi-branch crack in the NH specimen was observed along 240 frames, while the smaller single-branch crack of the HIP-1800 sample was observed only along 20 frames. That is, XZ-crack lengths of about 525 μm in as-printed parts, can be reduced to about 75 μm after HIP-1800 treatment. This indicates that HIP-1800 treatment can be used to passivate and mechanically heal crack clusters transverse to the build direction (i.e., in the XY-plane) and reduce XZ-crack length in the build direction by about 45 % and 85 %, respectively. Similar behaviour was observed in HIP-1800 L-PBF W reported in the literature, where surface cracks were healed by HIP-1800 treatment, significantly improving thermal conductivity [21]. Reduced solid-state cracking in both XY and XZ planes is expected to reduce variability in the tensile stress–strain performance of HIP-treated samples in comparison with the as printed NH condition. This is investigated in the following section.

The role of HIP treatment in healing process induced defects and solid-state cracking was investigated by interrogating XCT data for the different matchstick samples. XCT data from a 20 mm-length section was extracted from the mid-height of each 76 mm-long matchstick for image processing and quantitative analysis. Fig. 7a presents XCT images of all samples showing all the cracks, pores, lack of fusion, and edges scanned across the volume of the samples, projected on one single plane. Two orthogonal planes are shown for each sample in Fig. 7a. Fig. 7b shows void % measured for the different samples, which includes cracks, pores, and lack of fusion defects. To remove false positives, a filter was applied to look only at voids with dimension >0.002 mm^3. This was used to ignore smaller features which were predominantly ring artifacts or 'noise' acquired due to XCT scanning of dense tungsten material. An error bar is added, reflecting the maximum variation observed when repeating the same void segmentation three times in the volume with the highest void content (as-built coupon).

The HIP-treated samples show significant decrease of void % in comparison with the as-printed condition, with HIP-1800 showing the highest part density. A few lack-of-fusion defects were observed in HIP-1600 sample, which were not observed in other HIP-treated samples. It is suggested that these defects were formed during the printing process as previously described. However, more work is needed to investigate the cause of localised lack-of-fusion defects in the HIP-1600 bar specimen.

Solid-state cracks that form at the core of the part developed after finishing the EB-PBF process, when the samples cooled-down below the DBTT [27]. It is evident in Fig. 7 that HIP treatment reduces the quantity of solid-state cracking as cracks are passivated and mechanically healed by the HIP-treatment process [21]. This is more pronounced at the highest HIP temperature of 1800 °C.

4.4. *Mechanical testing of specimens produced using conventional raster-scanning melting strategy*

4.4.1. *Effect of HIP treatment on room temperature tensile testing*

The effect of HIP treatment was investigated in RS specimens to understand its role in the RT tensile performance. Fig. 8 shows RT tensile test results for different HIP conditions. Some tensile specimens failed prematurely due to critical damage introduced during the sample preparation process, which caused premature cleavage fracture due to high notch sensitivity [14]. Fig. 8a shows data points of successful tests for specimens of different batches and HIP-treatment conditions. Linear trends are shown, which exhibit high fit-to-the-data in all samples with coefficient of determination $R^2 \geq 0.9$, where $R^2 = 1$ indicates that the trend can be perfectly explained without error. These were used to investigate the effect of HIP temperature in the RT tensile stress–strain behaviour.

Trends with higher repeatability were observed in all HIP-treated conditions. This is explained in terms of crystallographic orientation, dislocation density and process induced defects as they influence the stress–strain performance. For instance, the beam power and beam speed used in the RS parameters are known to develop tungsten

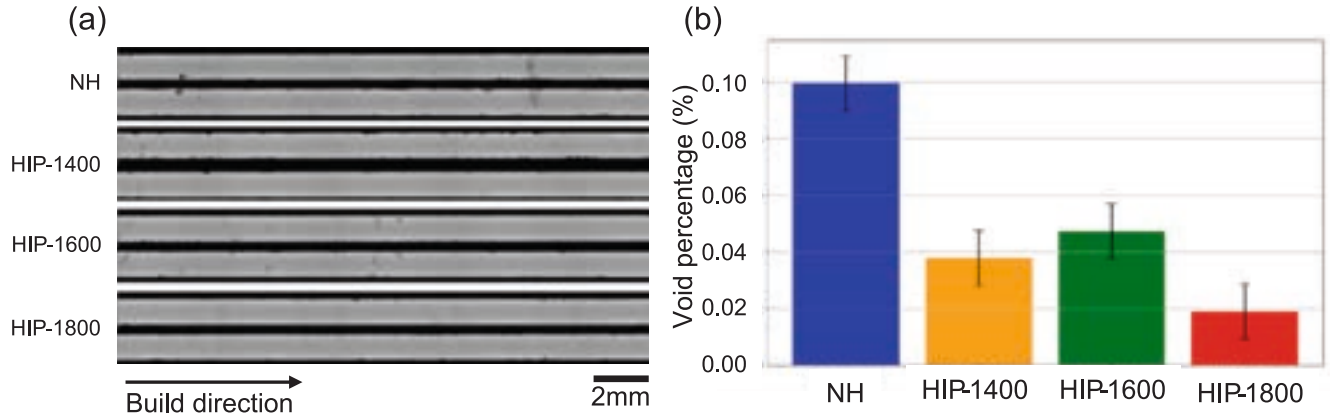

Fig. 7. (a) XCT images of as-printed and HIP-treated EB-PBF W matchstick specimens showing all the cracks and edges scanned across the volume of the samples, projected on one single plane. Two orthogonal planes are shown per sample. (b) Void percentage measured from all XCT specimens, which includes cracks, pores, and lack-of-fusion defects. A filter was applied to look only at voids with dimension >0.002 mm^3 to remove false positives and ignore smaller features which were predominantly ring artifacts or 'noise' acquired due to XCT scanning of dense tungsten material. All samples were printed using RS parameters.

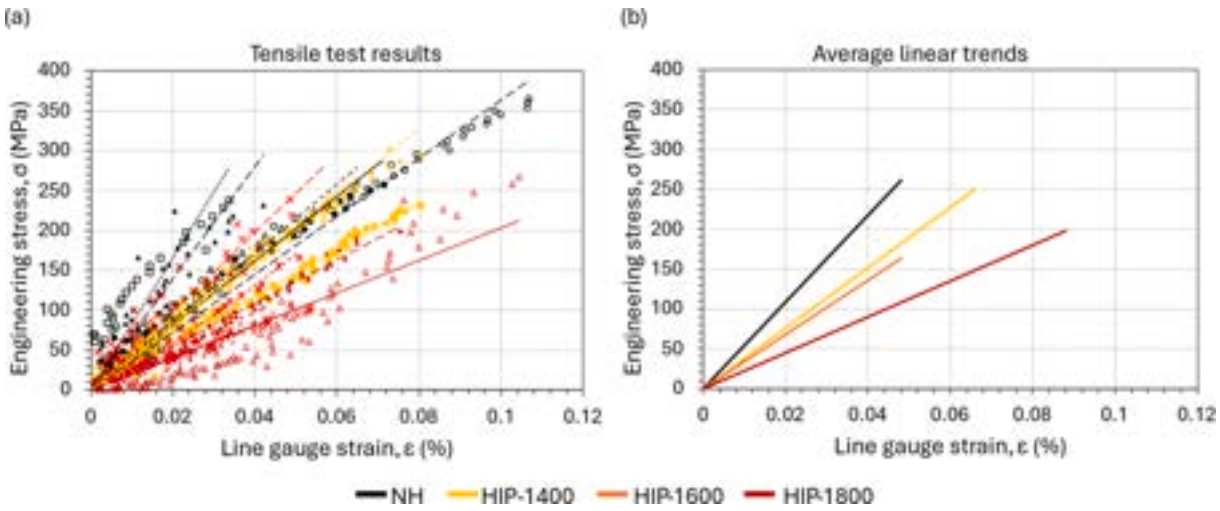

Fig. 8. (a) Stress–strain results from room temperature tensile tests measured using DIC. Different data points show the results from all the RS samples that were succesfully tested. Linear trends are shown for each sample. (b) Average linear trends up to median stress values calculated from the data points shown in a, for each HIP condition. The slope of the lines, which is associated with the Elastic Modulus, is reduced as HIP temperature increases. All samples were printed using RS parameters.

microstructures with fibre grains predominantly oriented in (111) and (001) [22]. From the stress–strain performance of single-crystal tungsten [14,53], it is known that tungsten crystals oriented in [001] show higher strain hardening (i.e., curves with a low slope) while crystals oriented in [111] exhibit more pronounced yield point (curves with a high slope) [14,48,49]. The as-printed RS samples show stress–strain curves with significant variation in the slope of the line, which indicate different stress–strain behaviour. It is hypothesised that this is caused by a combination of a) varying fraction of (111) and (001) crystallographic orientations and b) higher dislocation density with higher population of defects, which increase the scatter in as-printed RS specimens. It is thought that increased microcracking between pores in the NH specimens promote changes in the elastic modulus throughout the test, which is expected to further increase the scatter.

Since HIP-treatment reduces dislocation density and population of micro-pores and cracks [21,50], the repeatability of the stress–strain curve is expected to improve. This was observed in all HIP conditions as they show lower variation in the stress–strain behaviour.

Unexpectedly, lower stress–strain performance was observed in HIP-1600 samples, with higher variability compared with the other HIP conditions. It is thought that radiative cooling caused this anomaly by increasing defect population in this sample during the printing process. However, it is not clear as to why this happened considering the rolling order used. More work is needed to understand if the HIP-1600 lower performance was caused by anomalies during the HIP or EB-PBF process.

No significant variation was observed between batches b1 and b2 for any of the samples. This demonstrates uniform performance along the sample height, which indicates good thermal stability in the build direction.

Average linear trends are plotted up to median stress values in Fig. 8b. It is shown that the slope of the lines m, which is associated with the Elastic Modulus, reduces significantly as the HIP temperature is increased. Stiffer materials are described by higher Modulus, or higher m.

Fig. 9 plots average m values for the different HIP conditions against average grain width measured from tensile specimens. It must be noted that higher scatter in the stress–strain data shown in Fig. 8a may indicate increased microcracking, which is expected to induce constant changes

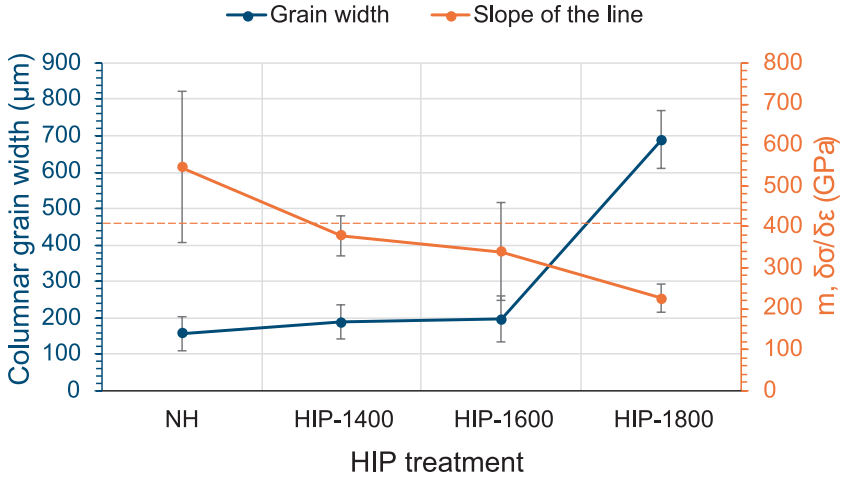

Fig. 9. Average grain width and slope of the line m of linear stress–strain trends for all HIP conditions. Trends of increasing grain width and decreasing m is observed with increasing HIP temperature. Error bars indicate the standard deviation of grain width measurements and m values calculated for each sample. Error bars in m indicate the variability of the stress–strain behaviour from tensile test results shown in Fig. 10a. Smaller error bars suggest higher repeatability of the stress–strain performance. All samples were printed using RS parameters. A dashed orange line indicates the Modulus of elasticity of tungsten taken from [51]. (For interpretation of the references to colour in this figure legend, the reader is referred to the web version of this article.)

in the Elastic Modulus throughout the test, in turn affecting average 'm' values. The Modulus of elasticity for conventional tungsten is 407.78 GPa [51]. This is used as reference to compare with the m data points in Fig. 9.

The slope variation observed in Fig. 8b is correlated with a grain coarsening trend, which is illustrated in Fig. 9. It is shown that m decreases with increasing grain width, indicating lower stiffness in coarser microstructures as HIP temperature is increased. It is noted that HIP-1400 and HIP-1600 reduce stiffness while maintaining relatively fine grain width of about $\leq$300 μm. On the other hand, extremely large grains are formed in the HIP-1800 sample further reducing stiffness. A critical m value is identified at the HIP-1800 sample, which describes an extremely coarse microstructure.

In Fig. 9, the error bars in m indicate the variability of the stress–-strain behaviour. Larger variability indicates lower mechanical stability. In general, the mechanical stability increases with increasing HIP temperature. As it is shown in Fig. 8, the as-printed samples exhibit the highest strength. However, as Fig. 9 indicates, they also exhibit the highest variability. On the other hand, HIP-1800 treatment improves the mechanical stability at the expense of extreme grain growth. More work is needed to develop optimal HIP parameters to find the best compromise between strength, grain size, and mechanical stability.

Vickers hardness tests were carried out to further investigate the varying stiffness behaviour. As expected, decreasing hardness was observed with increasing HIP temperature as No-HIP, HIP-1600, and HIP-1800 samples showed hardness of 393 $\pm$ 1 HV, 363 $\pm$ 10 HV, and 352 $\pm$ 5 HV, respectively. This explains the trend of decreasing stiffness observed in Fig. 9. Elevated temperature tensile testing is needed to further investigate the effect of varying grain size and elastic modulus in the stress–strain behaviour of ductile EB-PBF W specimens.

4.4.2. *Elevated temperature PIP testing*

Elevated temperature (ET) profilometry-based indentation plastometry (PIP) has been used before to provide outcomes that are in close agreement with those from tensile testing, concerning UTS, yield stress and work hardening [52]. ET-PIP was conducted here at 550 °C to investigate the relative performance between different HIP conditions. Two HIP-1800 specimens were tensile tested at the same temperature of 550 °C to obtain average results and compare against the corresponding PIP-tested sample.

Fig. 10 shows ET tensile and PIP-derived results. Premature failure occurred during ET-tensile testing due to out-of-plane displacement and wire-EDM-induced damage as previously described. However, ductile fracture was observed at this temperature, which enables comparison against the ET-PIP-derived performance of the HIP-1800 specimen. Good agreement was obtained between the PIP-derived yield stress (61 $\pm$ 16 MPa) and that obtained through ET-tensile testing (59 MPa).

PIP-derived UTS and yield strength can be used for relative comparison between the different HIP conditions investigated: PIP-derived UTS gradually reduces with increasing HIP temperature, while the PIP-derived yield strength reduces dramatically at the critical HIP temperature of 1800 °C, when excessive grain coarsening takes place. It is argued that PIP-derived yield strength can be used to differentiate performance of samples that exhibit significantly different grain size and stiffness.

It is known that HIP treatment gradually reduces Yield while increasing ductility in additively manufactured materials [53]. It is concluded that ET-PIP can be used as effective, low-cost testing method to support development of post-AM HIP treatment parameters. For instance, once EB-PBF parameters are developed for near-full density W parts, HIP temperature, pressure, and dwell time can be varied to develop a post-AM HIP-treatment process that maximises ductility while avoiding dramatic drop in the yield strength due to excessive grain coarsening. ET-PIP could be used to quickly assess PIP-derived yield strength to test a wider range of HIP-treated specimens for development of optimal HIP parameters.

Since the tensile sample fractured prior to necking, the UTS at fracture determined from the tensile test is significantly lower than the PIP-derived UTS which corresponds to the UTS at necking. Therefore, the two values are more difficult to compare. More ET-tensile testing is needed to evaluate the error magnitude of PIP-derived UTS results.

4.5. *Investigating alternative melting strategies for microstructure control*

In the previous section it was shown that higher crack density and larger crack length reduce the mechanical stability of EB-PBF tungsten parts. As these cracks are mechanically healed, the scatter of stress–-strain curves is reduced. In this section, different melting strategies are investigated using higher preheating temperature to reduce residual stresses and mitigate cracking in the as-printed condition. HIP-treatment is then used to investigate its effect on the new as-printed microstructures.

4.5.1. *Grain size and microstructure of as-printed parts produced by HP/HS-RS and SDS-PH strategies*

Raster scanning method with high beam power and high beam speed

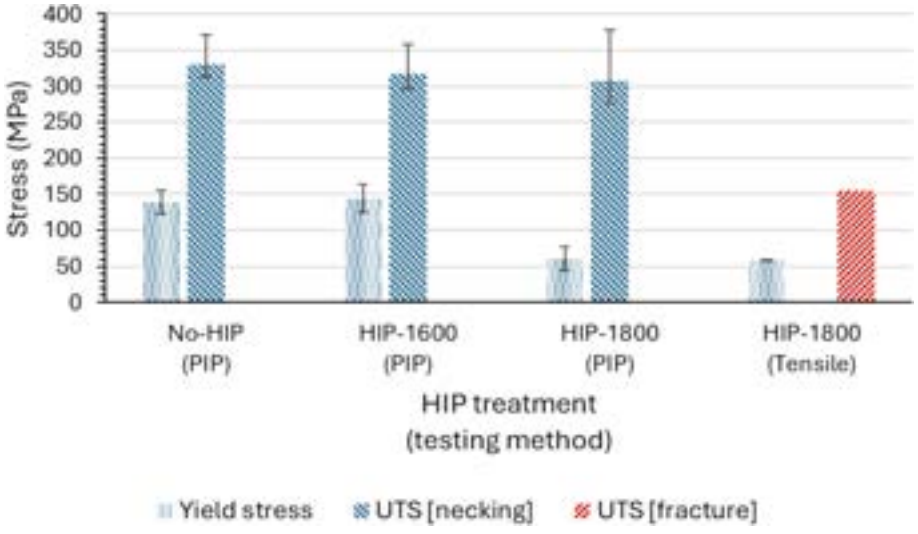

Fig. 10. Elevated temperature (550 °C) PIP-inferred and tensile strength results of EB-PBF W specimens printed with RS process parameters (see Table 3). All samples were printed using RS parameters.

(HP/HS-RS), and single directional shifted point heating source strategy (SDS-PH) were investigated for grain growth and cracking control. Beam power and beam speed are known to control grain size in PBF processes [54], and SDS-PH was demonstrated in [40] to control the microstructure of EB-PBF material. HP/HS-RS and SDS-PH tungsten samples were investigated and are shown against conventional raster scanning (RS) method for comparison.

It must be noted that HP/HS-RS and SDS-PH were developed using preheating temperature of 1200 °C, which is 200 °C higher than that used in the conventional RS strategy (See Table 3). This was used to mitigate larger thermal gradients expected as result of increasing beam power. High power necessitates high beam speed. At low velocities, there is sufficient time for heat to travel in the transverse direction during the melting process, increasing the local temperature which effectively serves as additional localised preheating. However, at high velocities this is greatly reduced, and additional local preheating is not possible. Therefore, higher substrate temperature is needed during the preheating process. Due to similar thermal gradient considerations, higher preheat temperature was used for both HP/HS-RS and SDS-PH.

HP/HS-RS was developed here for high productivity and high energy efficiency achieving a build rate of 5.45 cm^3/h and an energy consumption of 0.36 kWh/cm^3. In comparison to results obtained in [12], HP/HS-RS was 2.7 times faster and consumed 64 % less energy, whilst still achieving core relative densities of 99.62 % and 99.79 % in the XY and XZ planes respectively. SDS-PH was developed to reduce thermal gradients and cooling rates to control cracking, while achieving relative densities of about 99.8 % for both XY and XZ planes.

Fig. 11 shows the microstructure of (a, d) HP/HS-RS, (b, e) RS, and (c, f) SDS-PH samples in (a–c) XY and (d–f) XZ planes. Dark and light regions observed in optical micrographs indicate grains with different crystallographic orientation. This observation is further detailed in the following sections. In Fig. 11b, the XY plane of the RS sample shows evenly distributed grain orientation like that reported in [13], while HP/HS-RS and SDS-PH show stronger texture. This is in line with the processing map in [22] showing the fraction of fibre grains with varying beam parameters presented as higher beam power and higher beam speed promote stronger textures with predominantly (001) fibre grains in the build direction.

Fig. 11c shows SDS-PH square brick-shape texture due to the use of spot melting method. Since individual spots are melted separately following the single directional shifted order, they develop static melt pools (in contrast with the typical dynamic melt pools of conventional RS methods) that create a 'square brick' texture during solidification. Melt pool widths of about 270 μm can be measured from 'square bricks' in SDS-PH sample (see Fig. 11c) showing similar size to those of about 300 μ m-wide reported in the literature [22]. As wider melt pools are associated with reduced porosity [22] and fewer cracks [55], SDS-PH shows potential for reducing such process induced defects.

In the XZ plane, HP/HS-RS and SDS-PH show straight long columnar grains that grow along the entire sample height, whereas RS develops discontinuous columns undulating in the build direction that appear to break and merge. Wider columnar grains are evident in the SDS-PH sample, which indicates lower cooling rates and lower residual stresses. It is expected that different microstructures produced by different EB-PBF process parameters and different melting methods result in different mechanical performance. Pixelmelt® technology, an open code software, can be used to assign specific heating strategies in localised regions in the part to tailor microstructures and mechanical properties. In the present research, two different melting strategies are investigated separately to understand their effect on grain growth and cracking behaviour. Combined or more complex melting methods can be investigated in future work to further control microstructure and minimise cracking.

Fig. 12 shows columnar grain width for each build strategy (HP/HS-RS, RS, and SDS-PH). Micrographs of all melting strategies are inserted to illustrate columnar grains, and "sub-grains" defined by periodic

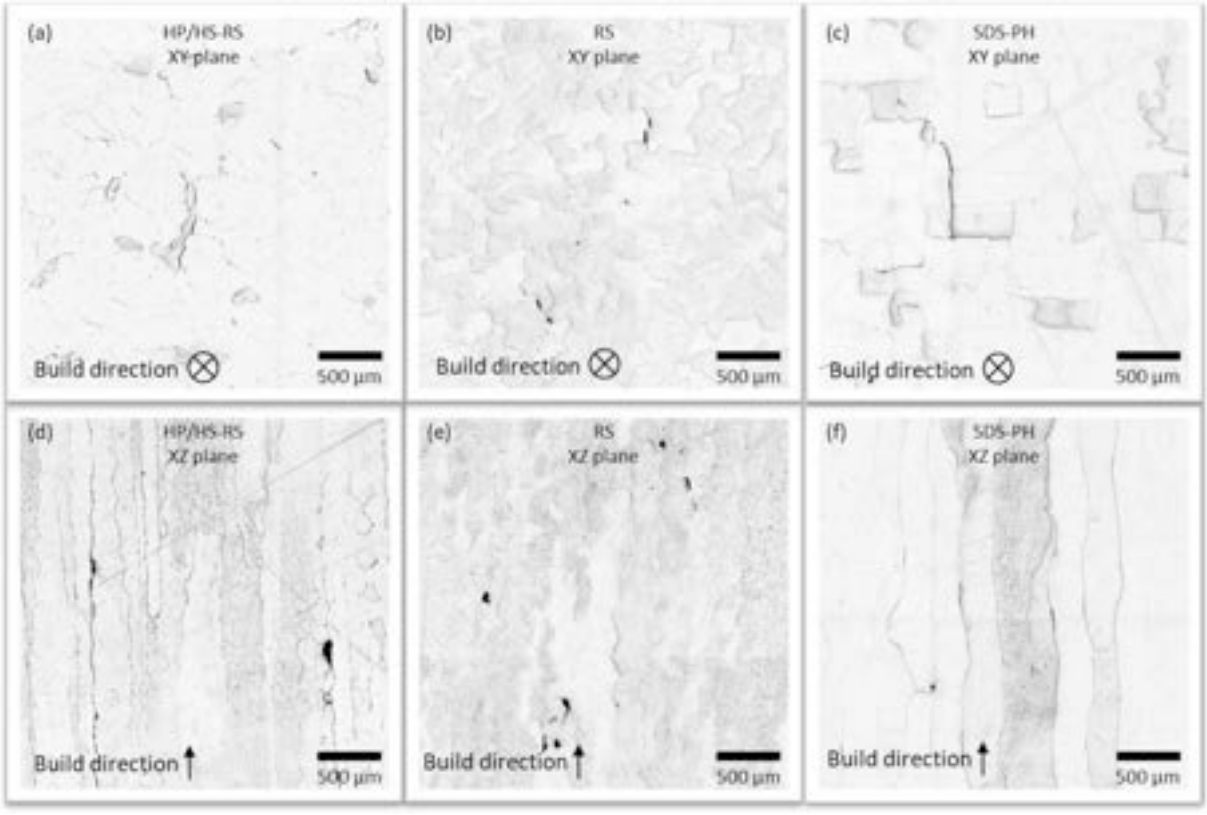

Fig. 11. Optical micrographs of (a, d) HP/HS-RS, (b, e) RS, and (c, f) SDS-PH specimens in (a–c) XY and (d–f) XZ planes.

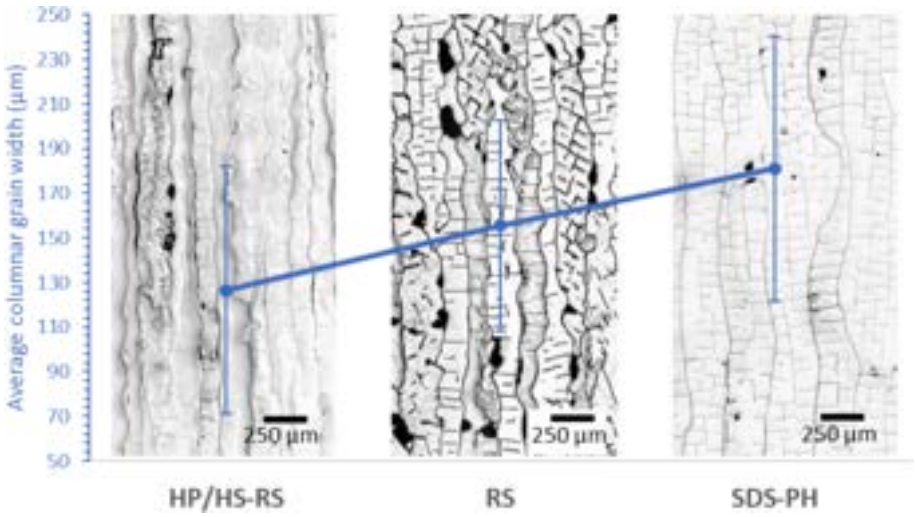

Fig. 12. Average columnar grain width measured from HP/HS-RS, RS, and SDS-PH specimens. Micrographs are shown which illustrate typical columnar grain structures for the different melting strategies. Grains and sub-grains are defined by periodic cracking caused by the wire-EDM sectioning process.

cracking in grain boundaries due to wire-EDM damage [14]. For SDS-PH, "sub-grains" describe same orientation across multiple columnar grains, while RS structures exhibit columnar grains with different orientation. It is known that grain boundaries with twist misorientation can form cracks when the angle of misorientation is more than about 8–10 degrees [56]. Dislocation mechanisms in tungsten often introduce weak boundaries and voids can easily nucleate at high angles of misorientation [57]. Reducing angles of misorientation is desired to control dislocation mechanisms and minimise cracking. It is argued that typical RS strategies induce higher angles of misorientation promoting crack nucleation in grain boundaries, possibly due to higher thermal gradients and cooling rates [58]. On the other hand, SDS-PH seems to promote uniform orientation which shows higher potential to reduce void nucleation and mitigate solid-state cracking.

It is shown in Fig. 12 that columnar grain width increases with varying melting strategy from HP/HS-RS to RS and SDS-PH respectively. Coarser microstructure of SDS-PH results from lower residual stress build-up as thermal gradients are controlled by use of point melting strategy, offering higher control of the process thermal distribution. For HP/HS-RS, finer microstructure is indication of higher residual stress build-up as high beam speeds are known to increase thermal gradients and cooling rates in PBF processes [59].

4.5.2. *Nanopore formation in as-printed material and mitigation through HIP-treatment*

Nanopore formation at grain boundaries is known to serve as crack nucleation points in AM W [27]. Nanopores can also affect the thermal properties in AM W components as they reduce the thermal diffusivity [60] of the printed parts as explained in [61]. HIP treatment was applied to HP/HS-RS and SDS-PH samples to investigate its potential to 'heal' or close such defects. Optical images in Fig. 13 show nanopores in the HP/HS-RS and SDS-PH samples for all HIP conditions. It is shown that nanopore formation at grain boundaries can be reduced with increasing HIP temperature for both HP/HS-RS and SDS-PH samples. Grains that were harder to polish were observed in all samples, which are depicted as rough dark regions in optical micrographs. These are denominated as 'rough' grains for simplicity.

4.5.3. *Texture observations from optical images*

Fig. 14 shows examples of XY and XZ optical micrographs of (a and b) HP/HS-RS and (c and d) SDS-PH samples. HP/HS-RS shows higher contrast between XY and XZ planes with significantly larger regions of rough grains in the XZ plane. Higher fraction of rough grains in the build direction, and smooth grains transverse to the build direction indicate high anisotropy in this material due to extremely strong texture. In contrast, SDS-PH shows more uniformly distributed grains of varying

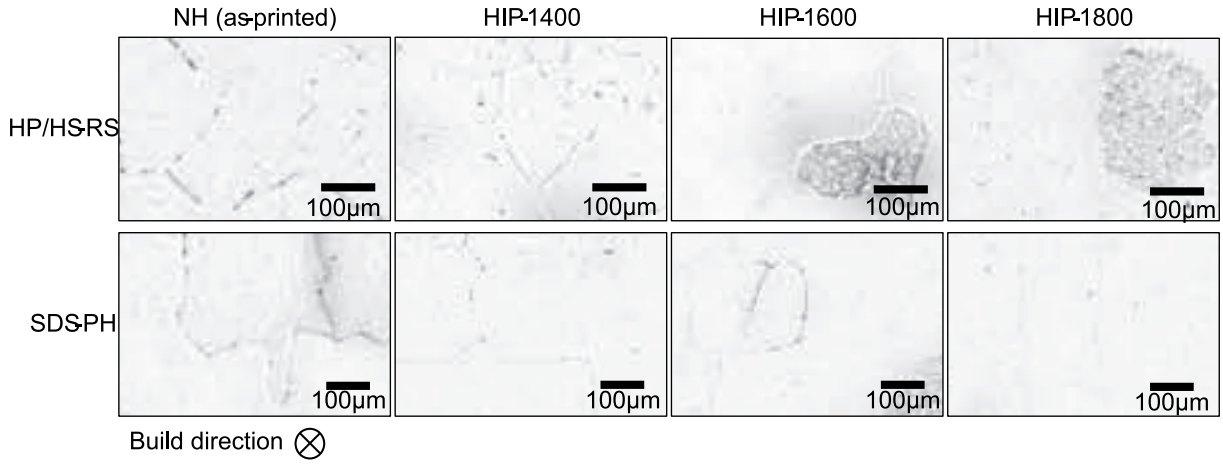

Fig. 13. XY micrographs of HP/HS-RS and SDS-PH specimens with varying HIP-treatment condition. Black arrows indicate nanopore segregationin grain boundaries. Nanopore segregation reduced with increasing HIP temperature.

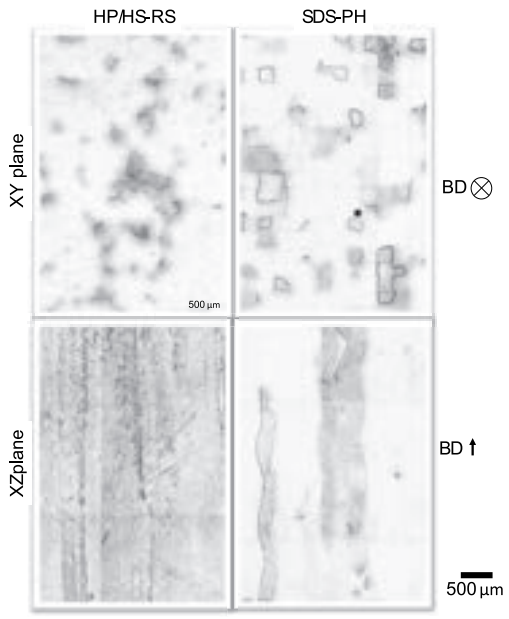

Fig. 14. Example of XY and XZ micrographs for HP/HS-RS and SDS-PH specimens. Dark regions indicate "rough" grains. High contrast between XY and XZ planes suggests higher anisotropy. BD indicates build direction.

"roughness" across XY and XZ planes, which indicates more isotropic characteristics. The same behaviour was observed in all HIP-treatment conditions.

To illustrate the texture and orientation of "smooth" and "rough" grains observed in optical micrographs, Fig. 15 shows optical, electron, forward scatter detector (FSD), inverse pole figure (IPF) and Euler colour images of the same sample. Black arrows indicate smooth-to-rough transitions in the optical micrograph, which correspond to locations of varying crystallographic orientation in IPF images and angles of orientation in Euler images. Electron images show fully dense material even around rough grains exhibiting dark boundaries in optical images, which demonstrates that dark boundary lines are not cracks. FSD images demonstrate rough surface associated with dark optical regions, and varying orientation and Euler angles characteristic of "rough" grains. It is noted that optical micrographs can provide information regarding locations where crystallographic orientation and Euler angles exhibit strong change.

It is known that reducing high angle grain boundaries (HAGBs) can help improve crack resistance and density [62]. IPF images in the build direction are used to identify HAGB regions as these are described by changes in the crystallographic orientation, e.g., from {001} to {111} and vice versa. A correlation between rough grains and {111} orientation in the build direction is identified. It is concluded that HAGB regions can be located around dark regions in optical micrographs, which are expected to increase cracking as they promote development of crack nucleation points.

4.5.4. *Cracking behaviour along columnar grains*

The cracking behaviour in the grain boundaries of SDS-PH and HP/HS-RS samples was investigated. Cleavage cracking was observed in {001} orientation relative to the build direction [14,63]. Fig. 16 shows FSD, electron, Euler colour, and IPF images in the build and transverse directions of HP/HS-RS and SDS-PH samples. FSD images illustrate some rough columnar grains and electron images show cracking around these grains. For SDS-PH, the rough grains are characterised by a change in the crystallographic orientation in the direction transverse to the build direction and a change in the Euler angles. In HP/HS-RS, an extremely strong texture characterised by a single crystalline-like structure was observed, where cracking is only described by strong changes in the Euler angles of orientation. It was found that HP/HS-RS develop extreme changes in the Euler angles demonstrating increased cleavage cracking in strong single crystalline-like textures around the boundaries of rough columnar grains. On the other hand, SDS-PH showed reduced cleavage cracking possibly due to more gradual changes in the Euler angles of a polycrystalline structure in transverse directions relative to the build direction.

4.5.5. *Cracking in samples produced by spot melting strategy*

As shown in Fig. 16, SDS-PH reduced cracking by controlling orientation changes. This is further investigated in XY and XZ planes to understand cracking behaviour in different regions of the part. Figs. 17 and 18 present micrograph mosaics of the entire cross-section. Electron and IPF images show microstructure and crystallographic orientations at centre and edge regions of the part. Electron images show near-full density especially in XZ plane; however, some micro-cracking is observed in the XY plane induced by changes in the crystallographic orientation. It is noted that the macro crack observed in Fig. 18a at the edge of the part developed when the sample was broken out of the hot mount in preparation for EBSD analysis.

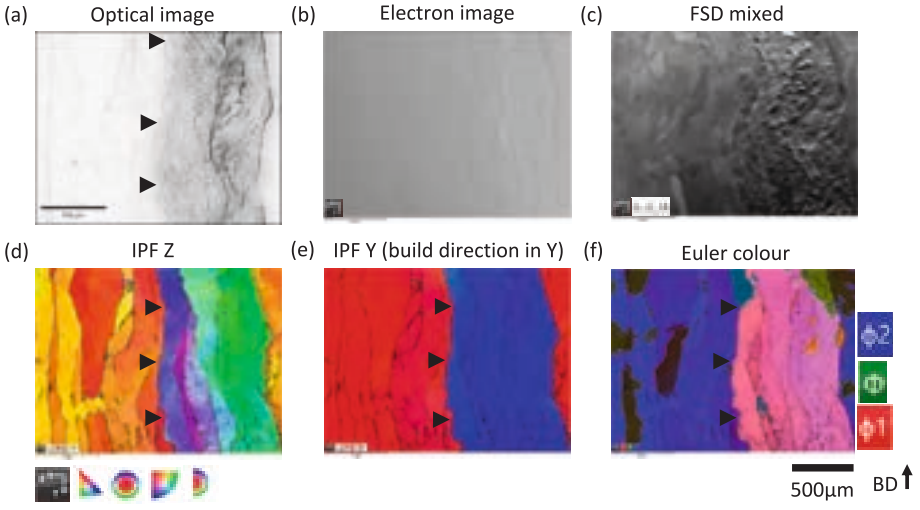

Fig. 15. (a) Optical, (b) electron, (c) forward scatter detector (FSD), (d, e) inverse pole figure (IPF) and (f) Euler colour images of the same SDS-PH HIP-1800 sample. Black arrows indicate location of white-dark boundaries from optical images and the corresponding colour change in IPF and Euler colour images. White-dark boundaries correspond to a change in crystallographic orientation from {001} to {111} in IPF Y image, respectively. BD indicates build direction.

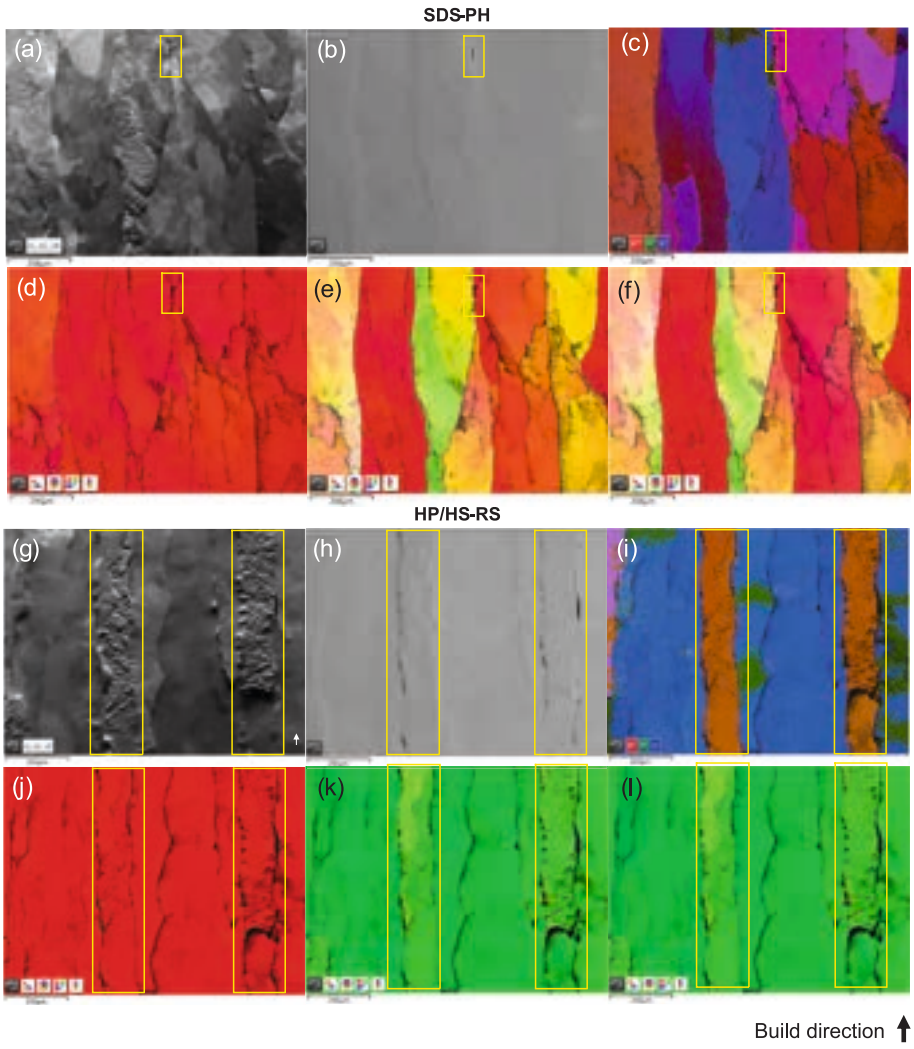

Fig. 16. (a, g) FSD, (b, h) electron, (c, i) Euler colour, and IPF images in (d, j) the build direction and (e, f, k, l) transverse directions for (a-f) SDS-PH and (g-l) HP/HS-RS samples, respectively. Location of cleavage cracking is indicated by yellow dotted rectangles. Build direction is indicated in Y axis. Scale bar in micrographs is 250 μm. (For interpretation of the references to colour in this figure legend, the reader is referred to the web version of this article.)

As previously explained, changes in the crystallographic orientations and Euler angles are described by light and dark changes in optical micrographs, with core regions predominantly oriented in {001} and {111}, respectively, relative to the build direction. The size of regions with {001} or {111} orientations in the build direction, can be measured from the optical mosaics. Larger and well-defined regions with uniform crystallographic orientation are produced by HIP-1800 treatment, increasingly forming single crystalline-like textures with more uniform orientation. A more homogenous optical mosaic suggests reduced variation in the Euler angles within single crystalline-like textures in the HIP-1800 sample.

The width of dark columnar grains with {111} orientation in the build direction, are shown from centre and edge locations in the as-printed sample measuring 252 μm and 218 μm, respectively (See Fig. 17a). For HIP-1800, larger {111} regions of 874 μ m- and 817 μm-wide are seen in centre and edge locations, respectively (See Fig. 17b). It is concluded that HIP-1800 treatment promotes stronger texture with more homogeneous orientation while increasing the width of single crystalline-like regions by about 3–4 times, in comparison with the as-printed condition (e.g., a 3396 μ m-wide region of uniform {001} orientation in the build direction, measured from the HIP-1800 sample is compared against a 1202 μ m-wide region measured from the as-printed condition).

In the XY plane transverse to the build direction, nano cracks (or voids) with potential to nucleate micro cracks are observed around grains predominantly oriented in {111}. These are indicated by white triangles in IPF images in Fig. 18a and b for the No-HIP and HIP-1800 samples, respectively. This is more clearly illustrated in Fig. 19 for the No-HIP condition, which shows core regions in the sample in more detail. IPF images in the build and transverse directions in Fig. 18 show that nano cracks nucleate predominantly around {111} grains, while larger micro cracks grow through grain boundaries between {001}-oriented grains in the build direction, and through grain boundaries between {011}- and {001}-oriented grains in directions transverse to the build direction. Even though HIP-1800 still shows multiple nano voids around {111} grains, it mitigated crack growth and virtually eliminated cracking in {011} and {001} regions, which demonstrates the capability of HIP-1800 for passivating and mechanically healing solid-state cracks in these regions. From optical mosaics, the as-printed material exhibits high population of square-shaped, dark grains mostly with {111} orientation and with size of about 245 μm × 265 μm, whilst HIP-1800 shows lower population of these {111}-oriented grains but larger in size with dimensions of about 598 μm × 586 μm. Dark grains are indicated by black triangles in optical mosaics in Fig. 18. For HIP-1800, larger areas of uniform orientations are expected to reduce the HAGB area and thus reduce formation of critical crack nucleation points.

Strong textures are observed in core regions of the XY plane, while more polycrystalline textures are observed at the edge regions of the

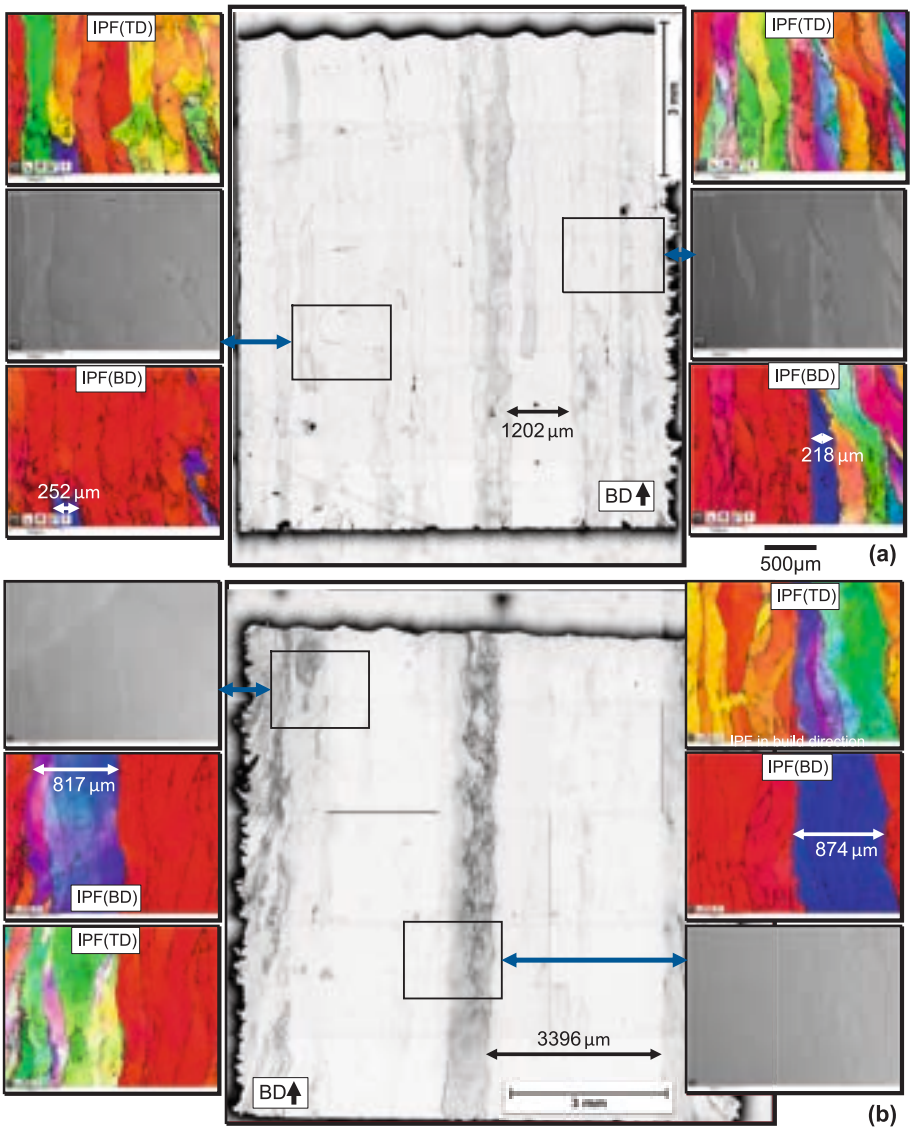

Fig. 17. Micrograph mosaic in XZ plane showing the entire cross-section of (a) SDS-PH No-HIP sample and (b) SDS-PH HIP-1800 sample. Electron and IPF images in the build (BD) and transverse (TD) direction show near-full density and crystallographic orientation respectively. Regions of {111} and {001} are shown by blue and red colours in IPF images, which correspond to darker and lighter regions in the optical mosaics, respectively. Widths of grains with {111} orientation are shown in IPF images and optical mosaic. The width of region with predominantly {001} orientation is shown in optical mosaic. A scale bar of 500 µm is shown which corresponds to all electron and IPF images. (For interpretation of the references to colour in this figure legend, the reader is referred to the web version of this article.)

part. This is explained in terms of different heat dissipation behaviour as the edge or contour regions are surrounded by powder which is known to have significantly lower thermal conductivity compared to the solidified material. This reduces local thermal gradients at the contour of the part, reducing the structure alignment in these regions.

A macro crack at the edge of the part is shown in Fig. 18a. This crack formed when the sample was broken out of the hot mount and was aggravated by changes of crystallographic orientations. The crack caused high noise levels in the IPF images and therefore prevented more detailed analysis. To investigate cracking behaviour in the XY plane, IPF images in the build and transverse directions were taken at the centre of the SDS-PH No-HIP sample and compared against electron images in Fig. 19. Microcracks and nanovoids are visible at (a–d) ×60 and (–h) ×200 optical microscope magnification, respectively. Nanovoids form predominantly around grains with {111} orientation as indicated by white arrows in Fig. 19. These serve as nucleation points for microcracks that grow along grain boundaries between {011}- and {001}-oriented grains. It is concluded that the HAGB area around grains oriented in {111} determines the population density of potential crack nucleation points in the XY plane.

5. Conclusions

EB-PBF process is identified as a potential AM method for producing relatively strong W parts (max. room temperature tensile strength achieved at ~350 MPa). Elevated temperature HIP treatment was demonstrated to reduce process-induced defects and solid-state cracking in EB-PBF W material. It was observed that HIP-treatment reduced the variability of the stress–strain curve, compared to the behaviour of as-printed specimens during room temperature tensile testing.

The detrimental effect of wire-EDM cutting on EB-PBF W specimens was identified as a significant challenge limiting proper evaluation of mechanical performance. It is concluded that the strong texture of EB-PBF W specimens with {001} orientation predominance is critically damaged by the wire-EDM process. This behaviour agrees with the literature, as wire-EDM is reported to cause periodic cracking especially along {001} planes.

Backscatter electron imaging was demonstrated as in-process non-

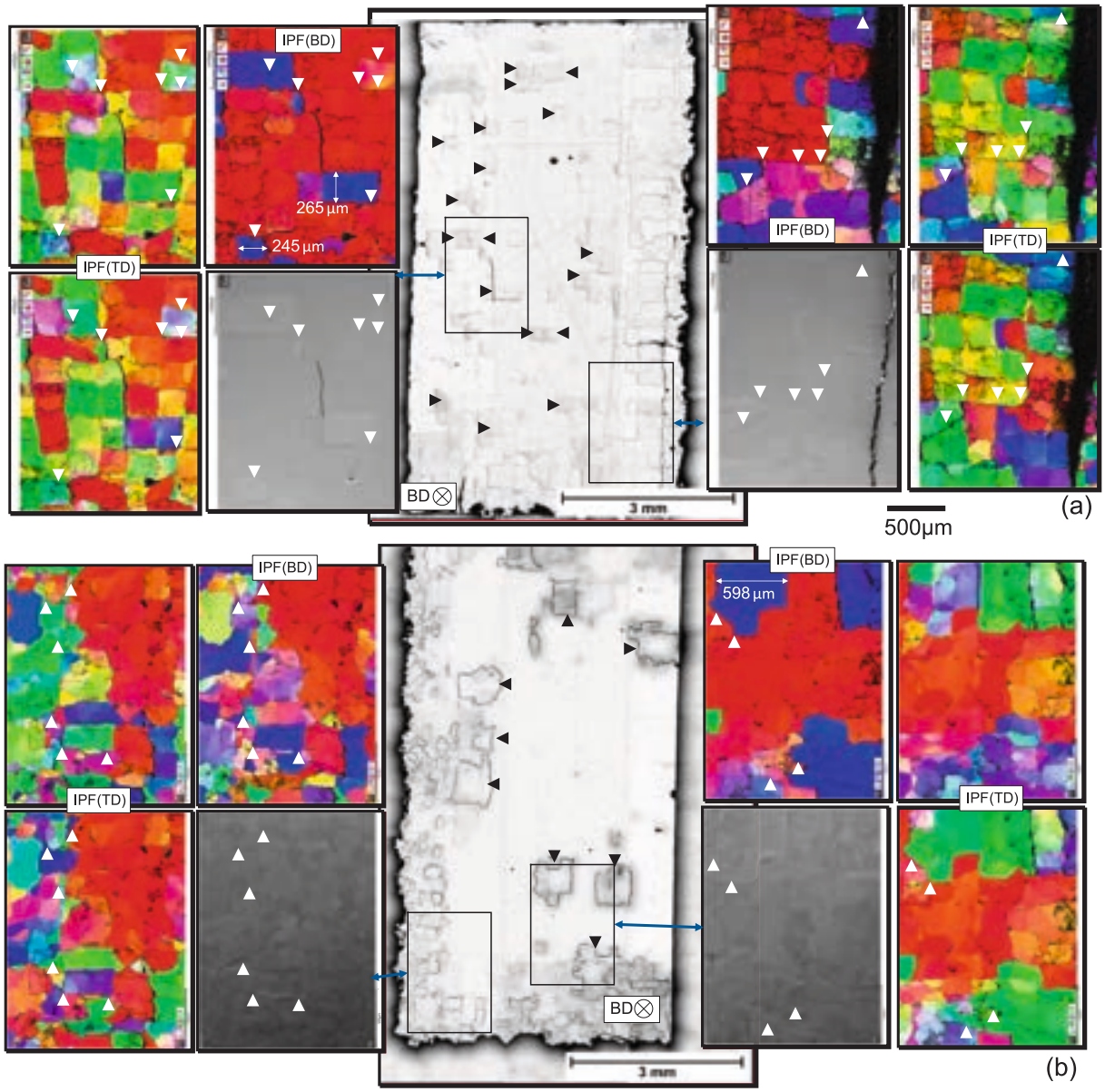

Fig. 18. Micrograph mosaic in XY plane showing the entire cross-section of (a) SDS-PH No-HIP sample and (b) SDS-PH HIP-1800 sample. Electron images show regions with near-full density and regions with cracking defects. IPF images show crystallographic orientation relative to the build direction (BD) and transverse direction (TD). Blue and red regions with {111} and {001} crystallographic orientation (relative to BD) correspond to dark and light regions in the optical mosaic, respectively. Widths of isolated grains with {111} orientation are shown in IPF images. Black arrows show locations of grains with predominantly {111} orientation relative to BD. White arrows show location of nanovoids. A scale bar of 500 µm is shown which corresponds to all electron and IPF images. (For interpretation of the references to colour in this figure legend, the reader is referred to the web version of this article.)

destructive evaluation tool for tungsten parts. It was used to conduct qualitative assessment of porosity layer by layer in the as-printed material. To the authors' knowledge, this is the first time that BSE imaging is used for in-situ quality control of tungsten in EB-PBF. BSE images with % porosity = 0, were correlated with near full density from optical micrographs.

XCT scanning was used to investigate cracking defects and voids in both as-printed and HIP-treated EB-PBF W specimens. It was found that higher HIP temperatures mechanically heal solid-state micro cracks located along grain boundaries between {011} and {001} oriented grains. It passivates crack clusters and reduces crack length in longitudinal and transverse directions relative to the build direction.

Elevated HIP temperatures were shown to close nanopores at grain boundaries, which is key to reduce crack nucleation points. Additional work is needed to further investigate the role of HIP treatment in the thermal properties and mechanical performance of EB-PBF W components. No mass deformation was observed after HIP treatment.

The potential of EB-PBF process to tailor W microstructures was demonstrated testing different manufacturing parameters and melting strategies. It was concluded that different melting strategies can be used to control grain growth and crystallographic orientation. Specimens with strong {001} crystallographic orientation were successfully produced, which shows potential of EB-PBF W material to improve PMI performance. Cleavage cracking in XZ plane was observed in {001} regions with strong change in the Euler angles of orientation. In the XY plane, nanovoids were observed around grains oriented in {111}. These serve as crack nucleation points for microcracks that grow transverse to the build direction, along grain boundaries in {011} and {001} oriented regions.

Higher crack density was observed in the XY plane (i.e.,

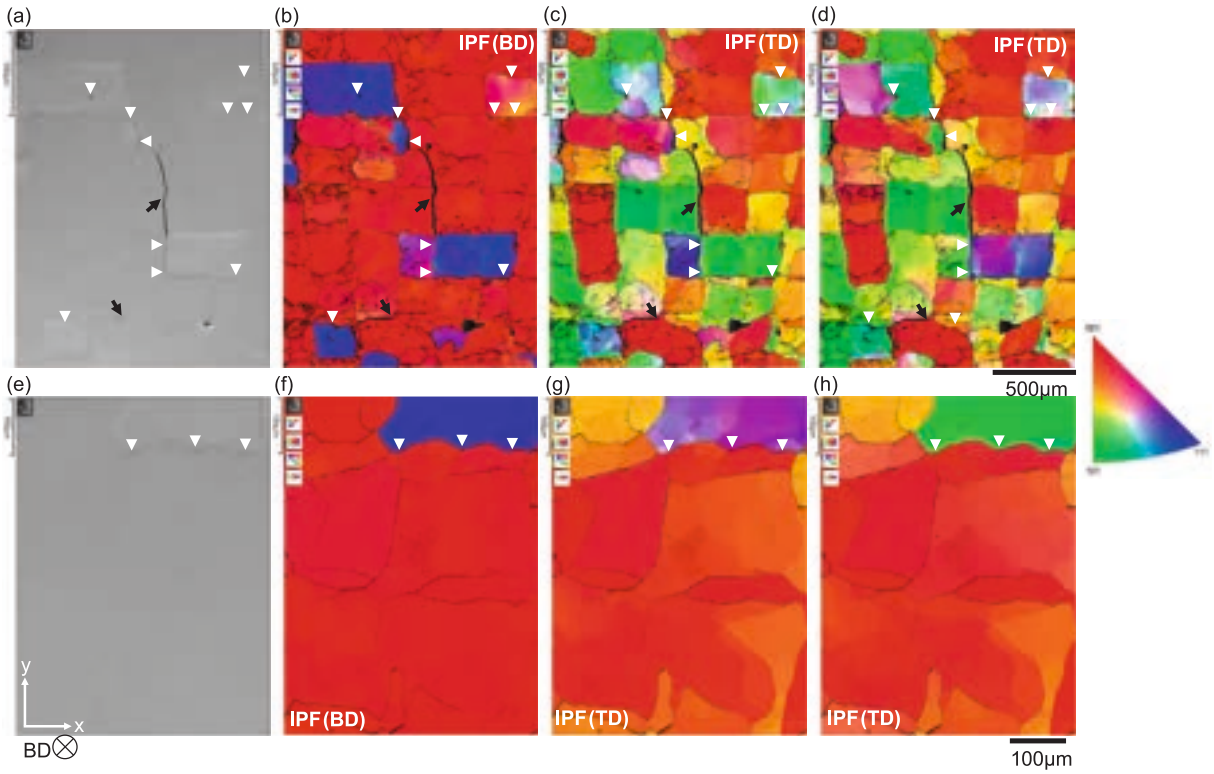

Fig. 19. (a, e) Electron and IPF images in (b, f) the build direction (BD) and (c, d, g, h) transverse directions (TD) of SDS-PH No-HIP sample at (a–d) 60× and (e–h) 200× optical microscope magnification, showing cracking in the XY plane perpendicular to BD. Black arrows show example of microcracks that grow in regions with {001} and {011} orientations. White arrows indicate location of nanovoids predominantly around {111} oriented grains. Microcracks are observed to nucleate from these nanovoids, which grow along grain boundaries between grains oriented in {011} and {001}.

perpendicular to the build direction) in comparison with the XZ plane (i.e., parallel to the build direction) due to increased number of HAGB regions around {111} oriented grains. Spot melting methods with at least 1200 °C preheating temperature is identified as a key melting strategy with potential to reduce crack nucleation points by: (a) promoting gradual change in the crystallographic orientation and Euler angles along the XZ plane (i.e., along the build direction), and (b) reducing the number of HAGB regions in the XY plane (i.e., transverse to the build direction). SDS-PH was demonstrated as one option to achieve this; however, a wide range of spot melting strategies and beam paths are available using Pixelmelt® technology which can be further explored to achieve higher control over grain growth and cracking behaviour.

CRediT authorship contribution statement

Miguel Zavala-Arredondo: Conceptualization, Methodology, Investigation, Writing – original draft, Writing – review & editing, Visualization. **Arun Ramanathan Balachandramurthi:** Investigation. **Lidija Stjepanic Peric:** Investigation. **Nick Weston:** Writing – review & editing, Investigation, Data curation. **Katy Rankin:** Writing – review & editing, Investigation, Data curation. **Sebastian Rosini:** Writing – review & editing, Investigation, Formal analysis, Data curation. **Khurram Amjad:** Writing – review & editing, Investigation, Data curation. **Jeong-Ha You:** Validation, Supervision, Funding acquisition.

Declaration of competing interest

The authors declare the following financial interests/personal relationships which may be considered as potential competing interests: Arun Ramanathan Balachandramurthi reports financial support was provided by Wallenberg Initiative Materials Science for Sustainability (WISE) funded by Knut and Alice Wallenberg Foundation. Arun Ramanathan Balachandramurthi reports a relationship with Freemelt AB. that includes: employment. Lidija Stjepanic Peric reports a relationship with Freemelt AB. that includes: employment. Arun Ramanathan Balachandramurthi has patent #SE2450809A1 – METHODS AND ARRANGEMENTS FOR CONTROLLING FUSION PARAMETERS IN ADDITIVE MANUFACTURING pending to BALACHANDRAMURTHI, Arun Ramanathan; ACKELID, Ulf. If there are other authors, they declare that they have no known competing financial interests or personal relationships that could have appeared to influence the work reported in this paper.

Acknowledgments

This work has been carried out within the framework of the EUROfusion Consortium, funded by the European Union via the Euratom Research and Training Programme (Grant Agreement No 101052200 — EUROfusion). Views and opinions expressed are however those of the author(s) only and do not necessarily reflect those of the European Union or the European Commission. Neither the European Union nor the European Commission can be held responsible for them. This work has also been part-funded by the EPSRC Energy Programme grant number EP/W006839/1. This work was partially supported by the Wallenberg Initiative Materials Science for Sustainability (WISE) funded by the Knut and Alice Wallenberg Foundation. We wish to acknowledge the Henry Royce Institute for advanced materials for enabling access to the AIP AIP8-45H HIP facility located at The Royce Translational Centre and the JEOL JSM-7900F SEM located in the Sorby Centre for Electron Microscopy, both at the University of Sheffield; EPSRC Grant Number EP/R00661X/1 & EP/P02470X/1). XCT was supported by the EPSRC National Research Facility for Lab X-ray CT (NXCT) at the μ-VIS X-ray Imaging Centre, University of Southampton, United Kingdom [EP/

T0259X/1].

Data availability

The authors do not have permission to share data.

References

[1] S. Wurster, et al., Recent progress in R&D on tungsten alloys for divertor structural and plasma facing materials, J. Nucl. Mater. 442 (1–3) (Nov. 2013) S181–S189, https://doi.org/10.1016/j.jnucmat.2013.02.074.

[2] International Tungsten Industry Association, "Applications & Markets," https://www.itia.info/applications-markets/.

[3] M. Richardson, et al., Technology readiness assessment of materials for DEMO in-vessel applications, J. Nucl. Mater. 550 (Jul. 2021) 152906, https://doi.org/10.1016/j.jnucmat.2021.152906.

[4] C. Luo, L. Xu, L. Zong, H. Shen, S. Wei, Research status of tungsten-based plasma-facing materials: a review, Fusion Eng. Des. 190 (May 2023) 113487, https://doi.org/10.1016/j.fusengdes.2023.113487.

[5] L. Cao, Z. Zhou, D. Yao, EAST Full Tungsten Divertor Design, J. Fusion Energ. 34 (6) (Dec. 2015) 1451–1456, https://doi.org/10.1007/s10894-015-9951-2.

[6] G.S. Xu, et al., Physics design of new lower tungsten divertor for long-pulse high-power operations in EAST, Nucl. Fusion 61 (12) (Dec. 2021) 126070, https://doi.org/10.1088/1741-4326/ac3297.

[7] P. Rindt, J. L. van den Eijnden, T. W. Morgan, and N. J. Lopes Cardozo, "Conceptual design of a liquid-metal divertor for the European DEMO," *Fusion Engineering and Design*, vol. 173, p. 112812, Dec. 2021, doi: 10.1016/j.fusengdes.2021.112812.

[8] P. Rindt, et al., Using 3D-printed tungsten to optimize liquid metal divertor targets for flow and thermal stresses, Nucl. Fusion 59 (5) (May 2019) 054001, https://doi.org/10.1088/1741-4326/ab0a76.

[9] B. Xiao, W. Jia, H. Tang, J. Wang, L. Zhou, Microstructure and mechanical properties of a newly developed WTaRe refractory alloy by selective electron beam melting, Addit. Manuf. 54 (Jun. 2022) 102738, https://doi.org/10.1016/j.addma.2022.102738.

[10] A. Talignani, et al., A review on additive manufacturing of refractory tungsten and tungsten alloys, Addit. Manuf. 58 (Oct. 2022) 103009, https://doi.org/10.1016/j.addma.2022.103009.

[11] Z. Hu, et al., Achieving high-performance pure tungsten by additive manufacturing: Processing, microstructural evolution and mechanical properties, Int J Refract Metals Hard Mater 113 (Jun. 2023) 106211, https://doi.org/10.1016/j.ijrmhm.2023.106211.

[12] D. Dorow-Gerspach, A. Kirchner, Th. Loewenhoff, G. Pintsuk, T. Weißgärber, M. Wirtz, Additive manufacturing of high density pure tungsten by electron beam melting, Nucl. Mater. Energy 28 (Sep. 2021) 101046, https://doi.org/10.1016/j.nme.2021.101046.

[13] S. Antusch, et al., Additive manufacturing of novel complex tungsten components via electron beam melting: basic properties and evaluation of the high heat flux behavior, Nucl. Mater. Energy 39 (Jun. 2024) 101683, https://doi.org/10.1016/j.nme.2024.101683.

[14] B. Butler, et al., Tensile deformation and failure of tungsten single crystals, Int J Refract Metals Hard Mater 110 (Jan. 2023) 106013, https://doi.org/10.1016/j.ijrmhm.2022.106013.

[15] S. Das, D.E.J. Armstrong, Y. Zayachuk, W. Liu, R. Xu, F. Hofmann, The effect of helium implantation on the deformation behaviour of tungsten: X-ray micro-diffraction and nanoindentation, Scr. Mater. 146 (Mar. 2018) 335–339, https://doi.org/10.1016/j.scriptamat.2017.12.014.

[16] S. Kajita, N. Yoshida, R. Yoshihara, N. Ohno, M. Yamagiwa, TEM observation of the growth process of helium nanobubbles on tungsten: Nanostructure formation mechanism, J. Nucl. Mater. 418 (1–3) (Nov. 2011) 152–158, https://doi.org/10.1016/j.jnucmat.2011.06.026.

[17] F.W. Meyer, et al., He-ion and self-atom induced damage and surface-morphology changes of a hot W target, Phys. Scr. T159 (Apr. 2014) 014029, https://doi.org/10.1088/0031-8949/2014/T159/014029.

[18] M. Alfazzaa, F. Pappalardo, A. Campos, G. Cartry, M. Minissale, C. Martin, Grain orientation and temperature dependences of bubbles at tungsten surfaces upon helium plasma exposure, Nucl. Mater. Energy 42 (Mar. 2025) 101883, https://doi.org/10.1016/j.nme.2025.101883.

[19] S. Das, H. Yu, E. Tarleton, and F. Hofmann, "Orientation-dependent indentation response of helium-implanted tungsten," *Appl Phys Lett*, vol. 114, no. 22, Jun. 2019, doi: 10.1063/1.5097403.

[20] H. Yu, S. Das, H. Yu, P. Karamched, E. Tarleton, F. Hofmann, Orientation dependence of the nano-indentation behaviour of pure Tungsten, Scr. Mater. 189 (Dec. 2020) 135–139, https://doi.org/10.1016/j.scriptamat.2020.08.014.

[21] J. Chen, et al., The effect of hot isostatic pressing on thermal conductivity of additively manufactured pure tungsten, Int J Refract Metals Hard Mater 87 (Feb. 2020) 105135, https://doi.org/10.1016/j.ijrmhm.2019.105135.

[22] C. Ledford, et al., Microstructure and high temperature properties of tungsten processed via electron beam melting additive manufacturing, Int J Refract Metals Hard Mater 113 (2023) 106148, https://doi.org/10.1016/j.ijrmhm.2023.106148.

[23] J.-H. You, H. Greuner, B. Böswirth, K. Hunger, S. Roccella, H. Roche, High-heat-flux performance limit of tungsten monoblock targets: Impact on the armor materials and implications for power exhaust capacity, Nucl. Mater. Energy 33 (Oct. 2022) 101307, https://doi.org/10.1016/j.nme.2022.101307.

[24] Z. Fu, C. Körner, Actual state-of-the-art of electron beam powder bed fusion, European Journal of Materials 2 (1) (2022) 54–116, https://doi.org/10.1080/26889277.2022.2040342.

[25] G. Yang, et al., Effect of processing parameters on the density, microstructure and strength of pure tungsten fabricated by selective electron beam melting, Int J Refract Metals Hard Mater 84 (Nov. 2019) 105040, https://doi.org/10.1016/j.ijrmhm.2019.105040.

[26] Jonathan Wright, "Additive Manufacturing of Tungsten via Selective Laser Melting and Electron Beam Melting," University of Sheffield, 2019. Accessed: Oct. 21, 2022. [Online]. Available: https://etheses.whiterose.ac.uk/26247/.

[27] E.A.I. Ellis, et al., Processing of tungsten through electron beam melting, J. Nucl. Mater. 555 (2021) 153041, https://doi.org/10.1016/j.jnucmat.2021.153041.

[28] P. Fernandez-Zelaia, M. Kirka, Q. Campbell, J. Ortega Rojas, A. Marquez Rossy, and C. Ledford, "Electron Beam Powder Bed Fusion Additive Manufacturing of Refractory Metals," United States, 2021. [Online]. Available: https://www.osti.gov/biblio/1832704.

[29] X. Ren, H. Peng, J. Li, H. Liu, L. Huang, and X. Yi, "Selective Electron Beam Melting (SEBM) of Pure Tungsten: Metallurgical Defects, Microstructure, Texture and Mechanical Properties," *Materials*, vol. 15, no. 3, 2022, doi: 10.3390/ma15031172.

[30] S. Antusch, J. Reiser, J. Hoffmann, A. Onea, Refractory Materials for Energy applications, Energ. Technol. 5 (7) (2017) 1064–1070, https://doi.org/10.1002/ente.201600571.

[31] H. Zhang, et al., Microstructure and Elevated Temperature Flexure Testing of Tungsten Produced by Electron Beam Additive Manufacturing, JOM 75 (10) (Oct. 2023) 4094–4107, https://doi.org/10.1007/s11837-023-06045-5.

[32] X. Jiang, X. Wang, Y. Yuan, Y. Yang, S. Tang, Y. Han, Microstructure and strengthening mechanisms in fine-grained and high-strength tungsten heavy alloy with a non-equiatomic Ni5.5Fe2.5CoCr high-entropy binder, Mater. Sci. Eng. A 908 (Aug. 2024) 146769, https://doi.org/10.1016/j.msea.2024.146769.

[33] S.G. Jeong, et al., Effect of substrate yield strength and grain size on the residual stress of direct energy deposition additive manufacturing measured by neutron diffraction, Mater. Sci. Eng. A 851 (Aug. 2022) 143632, https://doi.org/10.1016/j.msea.2022.143632.

[34] S. Chowdhury, et al., Laser powder bed fusion: a state-of-the-art review of the technology, materials, properties & defects, and numerical modelling, J. Mater. Res. Technol. 20 (Sep. 2022) 2109–2172, https://doi.org/10.1016/j.jmrt.2022.07.121.

[35] C. He, W. Yu, Y. Li, Z. Wang, D. Wu, G. Xu, Relationship between cooling rate, microstructure evolution, and performance improvement of an Al–Cu alloy prepared using different methods, Mater. Res. Express 7 (11) (Nov. 2020) 116501, https://doi.org/10.1088/2053-1591/abc4f9.

[36] H. Javidrad, F. Güler, H. Aydin, B. Koc, Effect of heat treatment and hot isostatic pressing on the microstructure and mechanical properties of the directed energy deposition IN738LC and IN718: a comparative study, Mater Charact 227 (Sep. 2025) 115279, https://doi.org/10.1016/j.matchar.2025.115279.

[37] S. Chen, H. Gao, Y. Zhang, Q. Wu, Z. Gao, X. Zhou, Review on residual stresses in metal additive manufacturing: formation mechanisms, parameter dependencies, prediction and control approaches, J. Mater. Res. Technol. 17 (Mar. 2022) 2950–2974, https://doi.org/10.1016/j.jmrt.2022.02.054.

[38] B. Vrancken, R.K. Ganeriwala, M.J. Matthews, Analysis of laser-induced microcracking in tungsten under additive manufacturing conditions: Experiment and simulation, Acta Mater. 194 (Aug. 2020) 464–472, https://doi.org/10.1016/j.actamat.2020.04.060.

[39] L. van Belle, G. Vansteenkiste, J.C. Boyer, Investigation of Residual Stresses Induced during the Selective Laser Melting Process, Key Eng. Mater. 554–557 (Jun. 2013) 1828–1834, https://doi.org/10.4028/www.scientific.net/KEM.554-557.1828.

[40] M.M. Kirka, et al., Strategy for Texture Management in Metals Additive Manufacturing, JOM 69 (3) (Mar. 2017) 523–531, https://doi.org/10.1007/s11837-017-2264-3.

[41] A. R. BALACHANDRAMURTHI and U. ACKELID, "METHODS AND ARRANGEMENTS FOR CONTROLLING FUSION PARAMETERS IN ADDITIVE MANUFACTURING," SE2450809 A1, Apr. 10, 2025.

[42] T.W. Clyne, J.E. Campbell, M. Burley, J. Dean, Profilometry-Based Inverse Finite Element Method Indentation Plastometry, Adv. Eng. Mater. 23 (9) (2021) Sep, https://doi.org/10.1002/adem.202100437.

[43] C. Arnold, "Fundamental Investigation of Electron-Optical Process Monitoring in Electron Beam Powder Bed Fusion," Friedrich-Alexander-Universität Erlangen-Nürnberg, 2023. [Online]. Available: https://nbn-resolving.org/urn:nbn:de:bvb:29-opus4-216113.

[44] P. Steuer, A. Rebschläger, O. Weber, D. Bähre, The Heat-affected Zone in EDM and its Influence on a following PECM Process, Procedia CIRP 13 (2014) 276–281, https://doi.org/10.1016/j.procir.2014.04.047.

[45] J.P. Oliveira, A.D. LaLonde, J. Ma, Processing parameters in laser powder bed fusion metal additive manufacturing, Mater. Des. 193 (Aug. 2020) 108762, https://doi.org/10.1016/j.matdes.2020.108762.

[46] J. Punturat, V. Tangwarodomnukun, C. Dumkum, Surface characteristics and damage of monocrystalline silicon induced by wire-EDM, Appl. Surf. Sci. 320 (Nov. 2014) 83–92, https://doi.org/10.1016/j.apsusc.2014.09.074.

[47] M.R. Khosravani, F. Berto, M.R. Ayatollahi, T. Reinicke, Fracture behavior of additively manufactured components: a review, Theor. Appl. Fract. Mech. 109 (Oct. 2020) 102763, https://doi.org/10.1016/j.tafmec.2020.102763.

[48] E. J. Horwath, "High strain rate deformation of tungsten single crystals. Final report, August 1992-April 1994," United States, 1994. [Online]. Available: https://www.osti.gov/biblio/80550.

[49] L.M. Garrison, Y. Katoh, N.A.P.K. Kumar, Mechanical properties of single-crystal tungsten irradiated in a mixed spectrum fission reactor, J. Nucl. Mater. 518 (May 2019) 208–225, https://doi.org/10.1016/j.jnucmat.2019.02.050.
[50] Q. Shi, et al., Improved mechanical properties and thermal conductivity of laser powder bed fused tungsten by using hot isostatic pressing, Mater. Lett. 377 (Dec. 2024) 137335, https://doi.org/10.1016/j.matlet.2024.137335.
[51] Plansee SE, "Properties of tungsten." [Online]. Available: https://www.plansee.com/en/materials/tungsten/properties.html.
[52] J. E. Campbell *et al.*, "A Critical Appraisal of the Instrumented Indentation Technique and Profilometry-Based Inverse Finite Element Method Indentation Plastometry for Obtaining Stress–Strain Curves," *Adv Eng Mater*, vol. 23, no. 5, May 2021, doi: 10.1002/adem.202001496.
[53] T. Cegan, et al., Effect of Hot Isostatic Pressing on Porosity and Mechanical Properties of 316 L Stainless Steel Prepared by the Selective Laser Melting Method, Materials 13 (19) (Oct. 2020) 4377, https://doi.org/10.3390/ma13194377.
[54] N. Hassine, S. Chatti, L. Kolsi, Tailoring grain structure including grain size distribution, morphology, and orientation via building parameters on 316L parts produced by laser powder bed fusion, Int. J. Adv. Manuf. Technol. 131 (9–10) (Apr. 2024) 4483–4498, https://doi.org/10.1007/s00170-024-13181-y.
[55] B. Vrancken, R. Ganeriwala, M. Matthews, Local strain release due to microcracking in laser melted tungsten, Procedia CIRP 111 (2022) 148–152, https://doi.org/10.1016/j.procir.2022.08.139.
[56] J. M. Liu and B. Whey Shen, "Crack nucleation in tungsten on crystallographic planes and on grain boundaries of twist misorientation," *Scripta Metallurgica*, vol. 17, no. 5, pp. 635–638, May 1983, doi: 10.1016/0036-9748(83)90392-7.
[57] Z. Zhou, et al., Grain structure and cracks behaviors of tungsten with different geometrical shapes and support structure prepared by laser powder bed fusion, J. Manuf. Process. 82 (Oct. 2022) 253–264, https://doi.org/10.1016/j.jmapro.2022.08.005.
[58] G. Mao, R. Cao, C. Cayron, X. Mao, R. Logé, J. Chen, Effect of cooling conditions on microstructures and mechanical behaviors of reheated low-carbon weld metals, Mater. Sci. Eng. A 744 (Jan. 2019) 671–681, https://doi.org/10.1016/j.msea.2018.12.035.
[59] S. Yim, et al., Cracking behavior of Ti-48Al-2Cr-2Nb alloy in powder bed fusion electron beam melting process, J. Mater. Process. Technol. 320 (Nov. 2023) 118104, https://doi.org/10.1016/j.jmatprotec.2023.118104.
[60] N. Mantel, et al., Development and testing of an additively manufactured lattice for DEMO limiters, Nucl. Fusion 62 (3) (Mar. 2022) 036017, https://doi.org/10.1088/1741-4326/ac486a.
[61] J.H. You, et al., Limiters for DEMO wall protection: initial design concepts & technology options, Fusion Eng. Des. 174 (Jan. 2022) 112988, https://doi.org/10.1016/j.fusengdes.2021.112988.
[62] T. Todo, T. Ishimoto, O. Gokcekaya, J. Oh, T. Nakano, Single crystalline-like crystallographic texture formation of pure tungsten through laser powder bed fusion, Scr. Mater. 206 (Jan. 2022) 114252, https://doi.org/10.1016/j.scriptamat.2021.114252.
[63] V. Glebovsky, H. Fishmeister, J. Riedle, V. Semenov, P. Gumbsch, The Influence of Crystallographic Orientation of the Crack Plane and Crack Front on the Fracture of Tungsten Single Crystals, MRS Proc. 367 (Sep. 1994) 141, https://doi.org/10.1557/PROC-367-141.